JOURNAL OF GEOPHYSICAL RESEARCH, VOL. 114, F03015, doi:10.1029/2008JF001137, 2009

Saturation of curvature-induced secondary flow, energy losses, and turbulence in sharp open-channel bends: Laboratory experiments, analysis, and modeling

K. Blanckaert[1,2]

Received 14 August 2008; revised 24 April 2009; accepted 4 June 2009; published 27 August 2009.

[1] The paper investigates the influence of relative bend curvature on secondary flow, energy losses, and turbulence in sharp open-channel bends. These processes are important in natural streams with respect to sediment transport, the bathymetry and planimetry, mixing and spreading of pollutants, heat, oxygen, nutrients and biological species, and the conveyance capacity. Laboratory experiments were carried out in a configuration with rectangular cross section, consisting of a 193° bend of constant radius of curvature, preceded and followed by straight reaches. This somewhat unnatural configuration allows investigating the adaptation of mean flow and turbulence to curvature changes in open-channel bends, without contamination by other effects such as a mobile bed topography. Experiments were carried out for three different values of the curvature ratio, defined as the ratio of centerline radius of curvature over flow depth, which is the principal curvature parameter for hydrodynamic processes. Commonly used so-called linear models predict secondary flow to increase linearly with the curvature ratio. The reported experiments show that the secondary flow hardly increases in the investigated very sharp bends when the curvature ratio is further increased. This phenomenon is called saturation. Similar saturation is observed for the energy losses and the turbulence. This paper focuses on the analysis and modeling of the saturation of energy losses and turbulence. Secondary flow is found to be the dominant contribution to the curvature-induced increase in turbulence production, which leads to increased energy losses. The curvature-induced turbulence is explained by the fact that the turbulence dissipation lags behind the turbulence production, in agreement with the concept of the turbulence energy cascade. A 1-D model is proposed for the curvature-induced energy losses and turbulence. It could extend 1-D or depth-averaged 2-D models that are commonly used in long-term (scale of a flood event to geological scales) or large-scale (scale of a river basin) investigations on flood propagation, hazard mapping, water quality modeling, and planimetric river evolution.

Citation: Blanckaert, K. (2009), Saturation of curvature-induced secondary flow, energy losses, and turbulence in sharp open-channel bends: Laboratory experiments, analysis, and modeling, *J. Geophys. Res.*, *114*, F03015, doi:10.1029/2008JF001137.

1. Introduction

[2] The sustainable development and exploitation of water resources is a prerequisite for the welfare of future generations. The wish and need to give more freedom to the river while maintaining its principal economical and sociological functions, calls for ever more subtle measures that intelligently influence the fluvial system rather than forcing it. The development of a generic insight and reliable engineering and management tools for natural river environments is complicated by the wide variety of encountered planimetries and scales, which renders the definition of a representative configuration impossible. To circumvent this problem, a research program is carried out that focuses on river meanders, which are typical and widespread elements in natural streams characterized by a distinctive interaction between hydrodynamic, morphodynamic and ecological processes that may be representative for a wider range configurations in natural streams. This program follows a three-component methodology that combines laboratory experiments, field experiments and numerical modeling.

[3] The present paper is the part of a series that reports results of laboratory experiments in a sharply curved meander bend. Most foregoing research on open-channel bends was limited to weak and moderate curvatures. At present, models for river dynamics (water quality, hydrodynamics, morphodynamics and planimetry evolution) are

[1]ENAC, Ecole Polytechnique Fédérale, Lausanne, Switzerland.
[2]Faculty of Civil Engineering and Geosciences, Delft University of Technology, Delft, Netherlands.

0148-0227/09/2008JF001137$09.00

unable to explain some relevant processes observed in natural meander bends, especially at high curvature.

[4] Curvature-induced secondary flow (also called spiral flow, helical flow, or cross-stream circulation) redistributes velocity, boundary shear stress, and sediment transport, and thereby plays an important role in shaping the river bathymetry and planimetry. Moreover, secondary flow enhances mixing. *Van Bendegom* [1947], *Rozovskii* [1957], *Engelund* [1974], *Kikkawa et al.* [1976], *de Vriend* [1977], among others, have proposed models for secondary flow, which are at the basis of one-dimensional models for curvature-induced advective mixing [*Fischer*, 1969; *Krishnappan and Lau*, 1977], the transverse bed slope and bathymetric characteristics in meander bends [*van Bendegom*, 1947; *Engelund*, 1974; *Kikkawa et al.*, 1976; *Odgaard*, 1981, 1982, 1984, 1986; *Struiksma et al.*, 1985], velocity redistribution [*Ikeda et al.*, 1981; *Odgaard*, 1986] and meander dynamics [*Ikeda et al.*, 1981; *Parker et al.*, 1982; *Parker et al.*, 1983; *Parker and Andrews*, 1986; *Furbish*, 1988; *Johannesson and Parker*, 1989b; *Seminara and Tubino*, 1992; *Liverpool and Edwards*, 1995; *Stølum*, 1996, 1998; *Edwards and Smith*, 2002; *Lancaster and Bras*, 2002].

[5] These models predict the secondary flow to grow proportionally to the relative curvature, parameterized by the ratio of flow depth to centerline radius of curvature, H/R. Their validity is limited to weak and moderate curvatures because they do not account for the feedback between streamwise flow and secondary flow, which is known to limit the growth of the secondary flow when the relative curvature increases. *Blanckaert and Graf* [2004] and *Blanckaert and de Vriend* [2003] have successfully explained and modeled this feedback in sharp bends. Their model could be used to extend the validity range of the aforementioned models for advective mixing, transverse bed slope, velocity redistribution, and meander migration.

[6] Existing models for meander dynamics overpredict the meander migration rate in the high curvature range and fail to simulate the reduced rates of bank erosion and meander migration at high curvature, as observed by *Hickin* [1974], *Hickin and Nanson* [1975], *Nanson and Hickin* [1986], *Hooke* [1987], *Biedenharn et al.* [1989]. *Bagnold* [1960] suggested that the maximum migration rate corresponds to minimum flow resistance related to flow separation. *Parker and Andrews* [1986] postulated as possible causes local obstructions in the floodplain, interactions between nonperiodic adjacent bends and higher-order flow interactions. *Markham and Thorne* [1992] focused on flow separation at the outer bank and the formation of embayments; *Sun et al.* [1996] attributed it to the interplay between the migrating river and the changing sedimentary environment created by the meandering river itself. *Seminara* [2006] and *Crosato* [2008] pointed to the importance of the spatial lag between the local curvature and the location of the maximum velocity excess. The limited growth of the secondary flow has not yet been investigated in detail, but is expected to contribute significantly to the reduced rates of bank erosion and meander migration at high curvature.

[7] Curvature-induced increase in turbulence leads to the increase in energy losses and results in enhanced mixing and spreading of pollutants, heat, oxygen, nutrients and biological species. Moreover, it increases the flow's capacity to erode and transport sediment as bed load or suspended load. Understanding of these processes is hampered by the almost complete lack of observations and detailed experimental data. Additional shear by the secondary flow and additional shear by horizontal velocity gradients, for example induced by zones of flow separation and recirculation, are known to generate additional turbulence in meander bends (K. Blanckaert, Topographic steering, flow recirculation, velocity redistribution and bed topography in sharp meander bends, submitted to *Water Resources Research*, 2009).

[8] Curvature-induced increase in energy losses reduces the conveyance capacity of rivers and channels. These have been studied by *Leopold et al.* [1960], *Onishi et al.* [1972], *Argawal et al.* [1984], and *Shiono et al.* [1999].

[9] These phenomena could possibly be accounted for and resolved by three-dimensional hydrodynamic numerical models with high spatial resolution and including a higher-order turbulence closure. But they are currently not accounted for in 1-D or 2-D depth-averaged morphodynamic models that are required, because of limitations in computational capacity, in long-term (scale of a flood event to geological scales) or large-scale (scale of a river basin) investigations on flood propagation, hazard mapping, water quality modeling, and planimetric river evolution. To date, such models are unable to describe curvature-induced turbulence and energy losses and they are limited to a simplified parameterization of the time-averaged flow based on a model for secondary flow which validity is limited to low and moderate curvatures.

[10] The present paper focuses on flow phenomena in the central part of the river. It does not investigate processes related to the interaction with the banks, such as flow separation and recirculation at the inner bank [*Leeder and Bridges*, 1975; *Andrle*, 1994; *Ferguson et al.*, 2003] and the counterrotating outer bank cell of secondary flow at the outer bank [e.g., *Mockmore*, 1943; *Bathurst et al.*, 1979; *Blanckaert and de Vriend*, 2004], which are known to be also important with respect to energy losses, turbulence production and meander migration. The present paper has the following objectives:

[11] 1. To report experimental data on the adaptation of secondary flow, turbulence, and energy losses to changes in curvature by means of laboratory experiments carried out at three relative curvatures corresponding to sharply curved flow. More particularly, the paper aims at illustrating that curvature-induced secondary flow, turbulence and energy losses tend to saturate at high relative curvature, which means that they hardly grow anymore when the relative curvature is increased, contrary to the growth proportional to the relative curvature that is predicted by "classical" models.

[12] 2. To interpret the data and to analyze the hydrodynamic mechanisms underlying and explaining the reported observations.

[13] 3. To propose 1-D models for the curvature-induced energy losses and turbulence that can be coupled to 1-D or 2-D depth-averaged morphodanymic models.

[14] 4. To provide high-quality data on the mean flow and turbulence that may be useful for model validation.

[15] The experimental setup and conditions, the applied measuring techniques, estimations of the uncertainty in

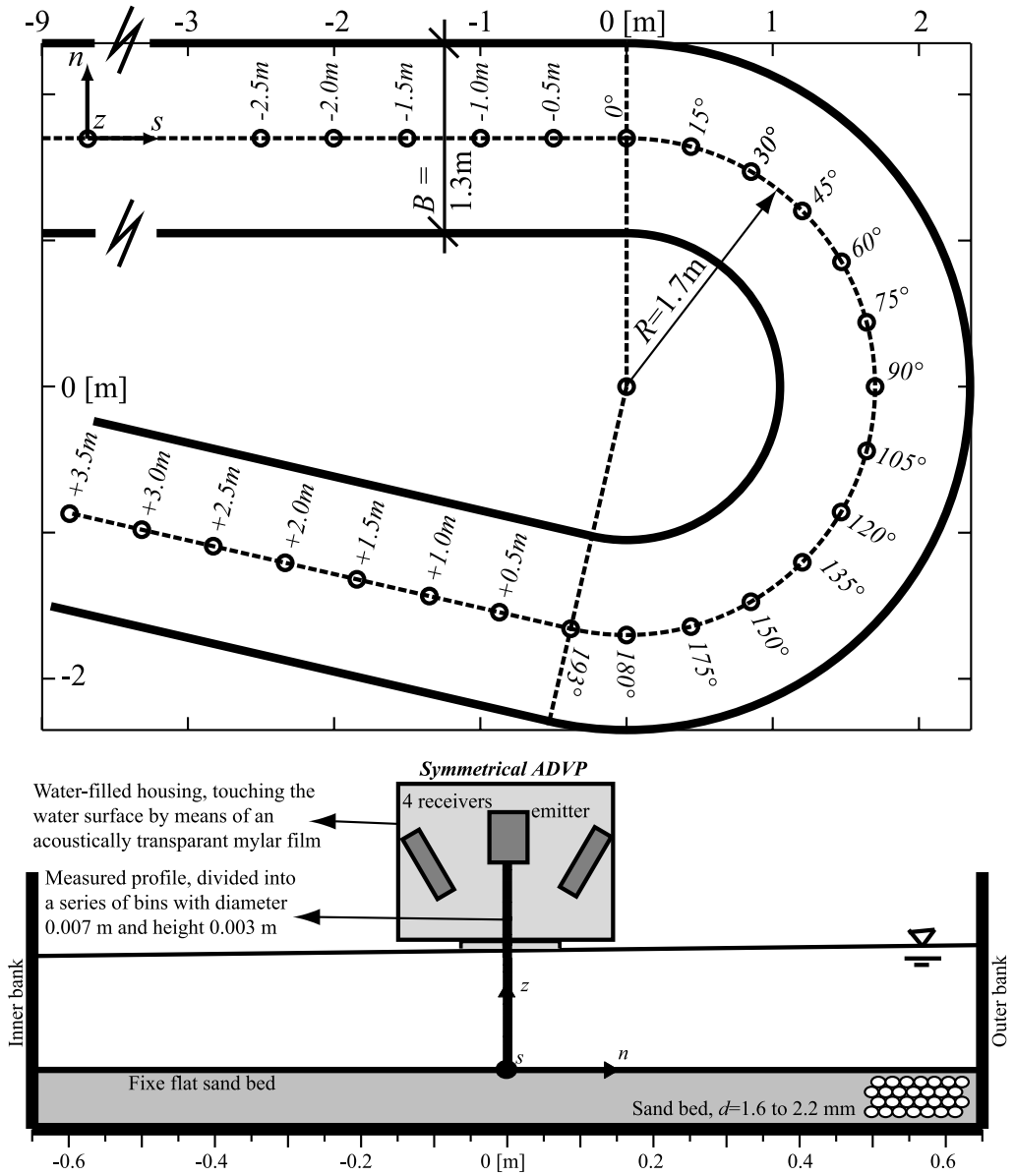

Figure 1. (top). Plan view of the laboratory flume. Dots indicate measured vertical profiles along the centerline in the M21_90_00, M16_90_00, and M11_90_00 experiments, respectively. (bottom) Cross section indicating the measured profile on the centerline and the Acoustic Doppler Velocity Profiler. Undistorted scales. Definition of the (s, n, z) reference system.

measured data and definitions of the secondary flow, and the relative curvature are reported and discussed in section 2 and subsequently one section is devoted to each of the objectives.

2. Experiments

[16] The experiments were carried out in the sharply curved laboratory flume shown in Figure 1. A 9 m long straight inflow reach allows the boundary layer to develop fully before the flow enters in the 193° bend of constant radius of curvature, R = 1.7 m, which is followed by a 5 m long straight outflow reach. The width of the flume is constant at B = 1.3 m. Quasi-uniform sand with diameters in the range d = 1.6 to 2.2 mm is glued on the horizontal bed, whereas the vertical banks are made of PVC.

[17] This laboratory flume has, on purpose, a simplified geometry that is not representative for natural streams:

[18] 1. The experiments were carried out over a horizontal bed, in order to isolate the influence of the relative curvature and avoid contamination by the interaction of the flow with a mobile bed topography. Moreover the horizontal bed topography strongly simplifies the cross-sectional patterns of secondary flow and turbulence variables, which can be represented by their centerline values. Therefore, the present paper will only report data measured on the centerline of the flume. Data measured in various cross sections through the bend that illustrate a more complete picture of the spatial

Table 1. Hydraulic and Geometric Conditions in the Series of Experiments[a]

Label	Q (ls^{-1})	$\tilde{H}$ (m)	$\tilde{U}$ (ms^{-1})	$E_{s,0}$ (10^{-4})	$C_{f,0}^{-1/2}$	$\tilde{E}_s$ (10^{-4})	$\tilde{C}_f^{-1/2}$	Re (10^3)	Fr	R/B	$R/\tilde{H}$	$B/\tilde{H}$
F_11_90_00	56	0.108	0.40	6.80	14.69	9.79	13.25	43	0.39	1.31	15.6	12.1
F_16_90_00	89	0.159	0.43	6.20	14.72	8.49	13.19	69	0.35	1.31	10.6	8.2
F_21_90_00	104	0.212	0.38	4.09	15.18	5.60	13.28	81	0.26	1.31	8.0	6.1

[a] Q is the flow discharge, $\tilde{H}$ is the flume-averaged flow depth, $\tilde{U} = Q/B\tilde{H}$ is the flume-averaged velocity, $E_{s,0}$ is the average energy slope in straight inflow, $C_{f,0}^{-1/2} = U_0/\sqrt{gR_{h,0}E_{s,0}}$ is a Chézy-type friction coefficient for the straight inflow based on the hydraulic radius R_h, $\tilde{E}_s$ is the flume-averaged energy slope, $\tilde{C}_f^{-1/2} = \tilde{U}/\sqrt{g\tilde{R}_h\tilde{E}_s}$ is a Chézy-type friction coefficient based on flume-averaged flow characteristics, $Re = \tilde{U}\tilde{H}/\nu$ is the Reynolds number, $Fr = \tilde{U}/\sqrt{g\tilde{H}}$ is the Froude number.

evolution of the hydrodynamics and that demonstrate the representativeness of centerline data have been reported by *Zeng et al.* [2008]. More three-dimensional velocity data can be obtained from the author.

[19] 2. The single-bend geometry is characterized by discontinuities in radius of curvature at the bend entry and exit, which are not representative for natural meander bends, but allow investigating in an isolated way the adaptation of the flow to changes in curvature as well as the recovery of the flow when the curvature vanishes.

[20] 3. The geometric simplicity makes for easier comparison with models.

[21] The geometric curvature in an open-channel bend depends on the centerline radius of curvature, R, the width of the flow, B and the depth of the flow, H, which can be combined into two independent dimensionless parameters, such as H/R and B/R. In natural streams R, B and H are correlated according to *Leopold et al.* [1960] and curvature can therefore be parameterized by one of the dimensionless parameters. Field studies typically make use of the dimensionless curvature ratio B/R. The parameters R, B and H are obviously not correlated in laboratory flumes. Since the parameter H/R is the principal curvature parameter in models for secondary flow, advective velocity distribution, transverse bed slope or mixing in open-channel bends (see section 1), it has been adopted in the present paper to parameterize relative curvature. All subsequent references to ''curvature'' or ''relative curvature'' mean H/R and not B/R. The reported experiments were designed so as to vary the overall averaged flow depth, $\tilde{H}$ and the relative curvature $\tilde{H}/R$, while keeping the bulk flow velocity, $\tilde{U} = Q/B\tilde{H}$ about constant.

[22] Data are represented and analyzed in a curvilinear reference system (s, n, z) with curvilinear s axis in streamwise direction along the centerline and taking its origin at the bend entry, transverse n axis to the left and vertically upward z axis (Figure 1). The transverse velocity component, v_n, is decomposed as [*Blanckaert and de Vriend*, 2003, Figure 1]

$$v_n = U_n + (v_n - U_n) \tag{1}$$

The depth-averaged transverse velocity U_n represents translatory cross flow, whereas $(v_n - U_n)$ represents the transverse component of the curvature-induced secondary flow, which is often called spiral flow, helical flow or cross-stream circulation. This decomposition of the transverse velocity and definition of the secondary flow are typical for laboratory studies. In field studies, secondary flow is often differently defined as the flow component perpendicular to the local depth-averaged flow.

[23] Table 1 summarizes the main hydraulic and geometric parameters of the experiments. Flow in all experiments is rough turbulent ($Re_* = u_*k_s/\nu > 70$ where Nikuradse's equivalent sand roughness k_s has been defined according to *van Rijn* [1984] as three times the sand diameter, $Re \gg 4000$), subcritical ($Fr < 1$), and very sharply curved ($R/B = 1.31$ and $R/\tilde{H} = 8.5$ to 15.6). The channel aspect ratio of $B/\tilde{H} = 6.1$ to 12.1 is rather high for a laboratory flume, but flow is still less shallow than in most natural rivers.

[24] In order to investigate and quantify the influence of curvature, characteristics of the straight flow in the inflow reach (labeled with the subscript *0*) will be adopted as reference values. Table 1 lists the energy slope in the straight inflow reach, $E_{s,0}$, which is computed from the measured water surface slope, $S_{s,0}$, as $E_{s,0} = S_{s,0}(1 - Fr_0^2)$. The roughness of the cross section is parameterized by the dimensionless Chézy coefficient defined as $C_{f,0}^{-1/2} = U_0/\sqrt{gR_{h,0}E_{s,0}}$, where U_0 and $R_{h,0}$ are the average velocity and hydraulic radius in the straight inflow, respectively.

[25] Owing to the horizontal bed, the cross-sectional averaged flow depth, $H(s)$, decreases slightly in streamwise direction, causing variations in the aspect ratio $B/H(s)$, the cross-sectional averaged velocity $U(s) = Q/BH(s)$ and the Froude number $Fr(s)$. Table 2 summarized extreme values of these variables at the flume's inlet and outlet, respectively. These variations do not fundamentally modify the hydrodynamics and do not alter the results and interpretations concerning the investigated processes. In order to avoid contamination by this variable flow depth in the data interpretation, mean velocities will be normalized in the present paper with the cross-sectional averaged velocity, $U(s) = Q/BH(s)$, whereas turbulence quantities will be normalized with the characteristic shear velocity for straight flow, defined as

$$u_{*,0}(s) = C_{f,0}^{1/2}U(s) \tag{2}$$

Table 2. Extreme Values of the Cross-Sectional Averaged Flow Depth, Channel Aspect Ratio, Flow Velocity, and Froude Number Occurring at the Flume's Inlet and Outlet[a]

	$H(s)$ (m)	$B/H(s)$ (−)	$U(s)$ (ms^{-1})	$Fr(s)$ (−)
	Inlet/Outlet	Inlet/Outlet	Inlet/Outlet	Inlet/Outlet
F_11_90_00	0.117/0.097	11.08/13.39	0.37/0.44	0.34/0.45
F_16_90_00	0.167/0.150	7.80/8.64	0.41/0.45	0.32/0.37
F_21_90_00	0.211/0.201	6.18/6.47	0.38/0.40	0.26/0.28

[a] $H(s)$, cross-sectional averaged flow depth; $B/H(s)$, channel aspect ratio; $U(s) = Q/(BH(s))$, the flow velocity; $Fr(s)$, the Froude number.

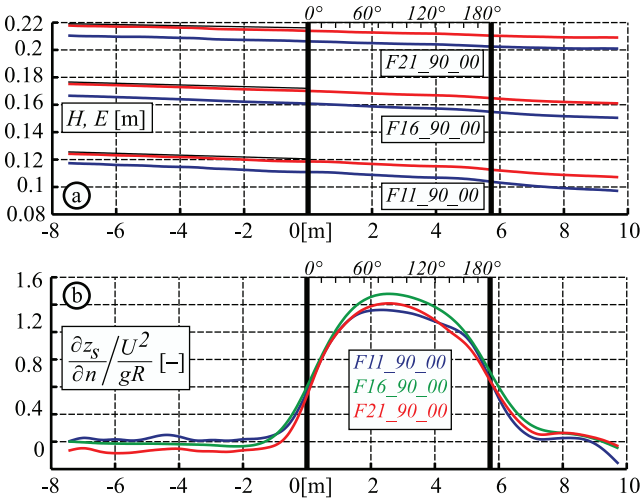

Figure 2. (a) Cross-sectional averaged water surface elevation, H (blue), cross-sectional averaged energy level, E (red), and linear fit of the energy level in the straight inflow reach (black) for the F11_90_00, F16_90_00, and F21_90_00 experiments; (b) Normalized transverse water surface slope, $\frac{\partial z_s}{\partial n}\Big/\frac{U^2}{gR}$, based on a linear approximation fitting to the measured water surface in the three experiments.

It should be noted that different methods can be applied to estimate the shear velocity in straight uniform flow (energy slope, logarithmic velocity profile, shear stress profile, turbulent kinetic energy). *Nezu and Nakagawa* [1993] describe these methods and estimate the uncertainty in the estimates as O(30%), which is in agreement with results from the presented experiments. Such an uncertainty is considerable, especially since most turbulence quantities are normalized with $u_{*,0}^2$.

[26] Measurements of the water surface topography were made by moving a set of 8 acoustic limnimeters mounted on a carriage along the flume. The limnimeters were mounted in the transverse positions n = [−0.6, −0.5, −0.3, −0.1, 0.1, 0.3, 0.5, 0.6] m. In streamwise direction, the measuring grid was refined near the bend entry and exit where important water surface gradients exist owing to the discontinuity in curvature. Measurements were made in the cross sections in the bend at [0, 5, 10, 15, 20, 25, 30, 35, 40, 50, 60, 70, 80, 90, 100, 110, 120, 130, 140, 150, 160, 165, 170, 175, 180, 185, 190, 193]° and in the straight outflow at [0.3, 0.5, 0.8, 1, 1.3, 1.5, 1.8, 2, 2.5, 3, 3.5, 4] m downstream of the bend. In order to estimate accurately the small water surface and energy slopes in the straight inflow reach, a refined measuring grid was adopted with 24 transverse measuring positions in cross sections spaced by 0.1 m in the reach from 7.5 m upstream of the bend entrance onto the bend entrance.

[27] Nonintrusive measurements of velocity profiles were carried out with an Acoustic Doppler Velocity Profiler (ADVP) on the centerline at 2.5 m, 2.0 m, 1.5 m, 1.0 m, 0.5 m upstream of the bend, every 15° in the bend and every 0.5 m in the straight outflow reach (Figure 1). The working principle of the ADVP has been reported by *Lemmin and Rolland* [1997], *Hurther and Lemmin* [1998], *Blanckaert and Graf* [2001], and *Blanckaert and Lemmin* [2006]. The ADVP consists of a central emitter, surrounded by four receivers, placed in a water filled box that touches the water surface by means of an acoustically transparent mylar film (Figure 1). It measures profiles of the quasi-instantaneous velocity vector, $\vec{v}(t) = (v_s, v_n, v_z)(t)$, from which the time-averaged velocity vector, $\overline{\vec{v}} = (\overline{v}_s, \overline{v}_n, \overline{v}_z)$, the Reynolds stresses, $-\rho\overline{v_i' v_j'}$ $(i, j = s, n, z)$ and higher-order turbulent correlations can be computed. Measurements were made with a sampling frequency of 31.25 Hz and a sampling period of 90 s. The series of experiments is designed to make optimal use of the ADVP's strong points, as explained by K. Blanckaert (submitted manuscript, 2009).

[28] Blanckaert (submitted manuscript, 2009) reports and illustrates the data treatment procedures applied to transform the raw data obtained by the ADVP into a format appropriate for data analysis and presentation. Moreover, he estimates the uncertainty in the experimental data as follows: streamwise velocity v_s: 4%, cross-stream velocities (v_n, v_z): 10%, shear velocity u_*: 30%, turbulent shear stresses: 15%, turbulent normal stresses and turbulent kinetic energy: 20% (accounting for noise corruption of high frequency fluctuations by means of the method reported by *Blanckaert and Lemmin* [2006]), turbulence production rate: 50% and turbulence dissipation rate: 100%.

[29] The accuracy in the ADVP measurements is reduced near the flow boundaries. At the water surface, the ADVP housing (Figure 1) perturbs the flow in a region of about 2 cm (about 10 to 15% of the flow depth in our experiments). In a flow layer of about 2 cm near solid boundaries, the ADVP seems to underestimate turbulent characteristics, which is tentatively attributed to the high velocity gradients within the measuring volume and/or to parasitical echoes from the solid boundary [*Hurther and Lemmin*, 2001]. ADVP measurements seem to underestimate systematically the vertical velocity fluctuations.

3. Experimental Observations

3.1. Water Surface Topography

[30] Figure 2 synthesizes the measured water surface topographies by means of the cross-sectional averaged water surface elevation, H (Figure 2a), and the normalized transverse water surface slope (also called superelevation), $\frac{\partial z_s}{\partial n}\Big/\frac{U^2}{gR}$ (Figure 2b). The measured cross-sectional averaged water surface elevation, H, allows estimating the cross-sectional averaged energy level, E (Figure 2a), the cross-sectional averaged streamwise energy gradient, E_s and the dimensionless Chézy coefficient, C_f, as detailed in section 2.

[31] Table 1 indicates that the overall averaged streamwise energy gradient $\tilde{E}_s$ is considerably higher than the streamwise energy gradient in the straight inflow reach E_{s0}: $\tilde{E}_s/E_{s0} \approx 1.44$, 1.37 and 1.37 in the F11_90_00, F16_90_00 and F21_90_00 experiments, respectively, resulting in a change of the dimensionless Chézy coefficient $C_f^{-1/2}$ of about 10%. Remarkably, these curvature-induced energy losses do not increase with the curvature ratio $\tilde{H}/R$ in the reported experiments but are about identical.

[32] The transverse tilting of the water surface has a similar behavior in the three experiments. It begins about 1m upstream of the bend entrance, increases about linearly in the first 30° of the bend and reaches its maximum values of $\frac{\partial z_s}{\partial n}\Big/\frac{U^2}{gR} \approx 1.4$ in the bend reach between 60° and 90°.

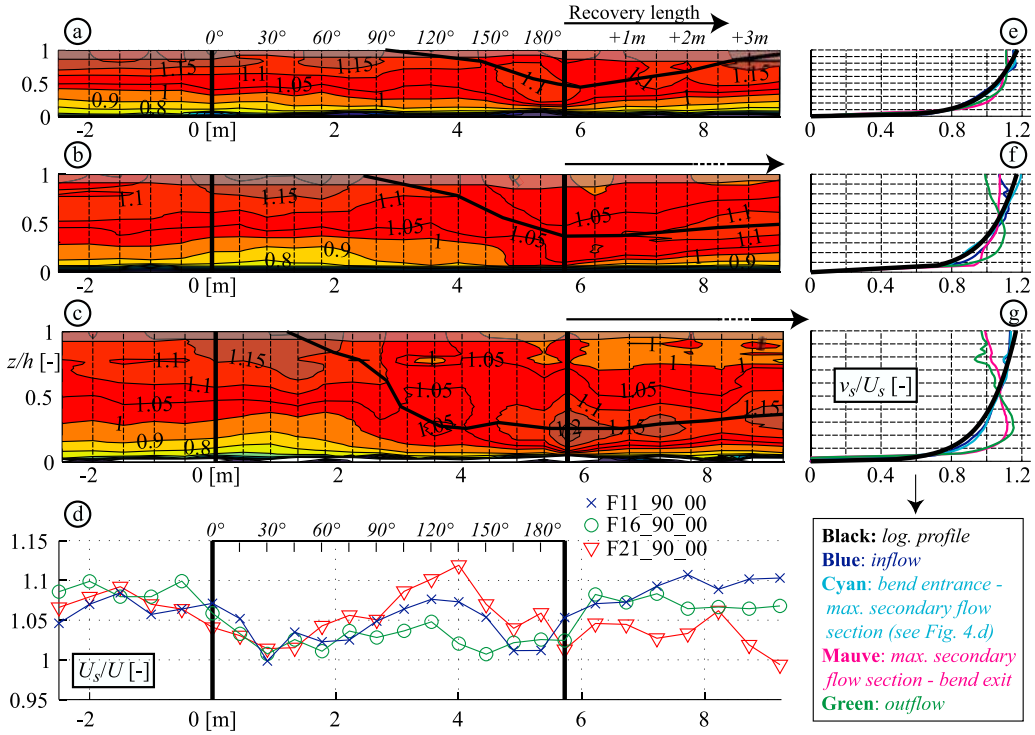

Figure 3. Isolines of the streamwise velocity normalized with the local depth-averaged streamwise velocity, v_s/U_s, along the centerline in (a) the F11_90_00 experiment, (b) the F16_90_00 experiment, and (c) the F21_90_00 experiment. The black line indicates approximately the location where $\partial v_s/\partial z = 0$. Measured data have been extrapolated in the shaded near-surface region. Figures 3a–3c are distorted by a factor 10. (d) Streamwise distribution along the centerline of the depth-averaged streamwise velocity normalized with the cross-sectional averaged streamwise velocity, U_s/U. (e–g) Vertical profiles of the normalized streamwise velocity, v_s/U_s, according to the indicated legend in the F11_90_00, F16_90_00, and F21_90_00 experiments, respectively.

Remarkably, the transverse tilting of the water surface slope does subsequently not remain constant in this long bended reach of constant curvature, but decreases and it is reduced at the bend exit to about half of its maximum value in the bend, indicating that the transverse tilting of the water surface overshoots its equilibrium value in the first part of the bend. The transverse tilting decays quickly downstream of the bend and is negligible about 1 m downstream of the bend exit. These observations deviate from the "classical" description of the transversal tilting as adapting very quickly to curvature changes and being constant in a bend of constant radius of curvature.

3.2. Mean Flow Characteristics Along the Centerline

[33] Figure 3 shows the evolution of the streamwise velocity along the centerline in the three experiments. Velocity profiles have been normalized with the local depth-averaged velocity, U_s, such that the depth-averaged value of all illustrated profiles is equal to 1.

[34] The evolution along the centerline of the streamwise velocity profiles is similar in all three experiments. The v_s profiles are about logarithmic in the straight inflow reach. In the first part of the bend, v_s slightly increases/decreases in the upper/lower part of the water column. Subsequently, the highest velocities plunge toward the bed, causing a decrease/increase of v_s in the upper/lower part of the water column, which is expected to cause an increase in bed shear stress. This process seems to be more pronounced and to start earlier in the bend with increasing curvature ratio, $\tilde{H}/R$. The v_s profiles recover toward their logarithmic form in the straight outflow reach, whereby the recovery length seems to increase with $\tilde{H}/R$. The depth-averaged velocity U_s (Figure 3d) only slightly varies along the centerline, which is due to redistribution of v_s in the cross section around the bend.

[35] Figure 4 summarizes the evolution along the centerline of the depth-averaged transverse velocity U_n, representing translatory cross flow, and the transverse component of the secondary flow, $(v_n - U_n)$ (equation (1)). The vertical velocity v_z (not shown) is negligible on the centerline, which indicates that the centerline is situated near the center of the secondary flow cell.

[36] The secondary flow has a similar evolution in all three experiments. It comes into existence at the bend entrance, increases in the first part of the bend, has maximum values in the bend reach between 60° and 135°, decreases in the second part of the bend and decays in the straight outflow (Figures 4a–4c). Figure 4d quantifies the evolution of the strength of the secondary flow by means of the parameter $\sqrt{\langle (v_n - U_n)^2 \rangle}/U$ (Brackets $\langle\ \rangle$ indicate depth-averaged values). Remarkably, the maximum secondary flow strength is comparable in all three experiments

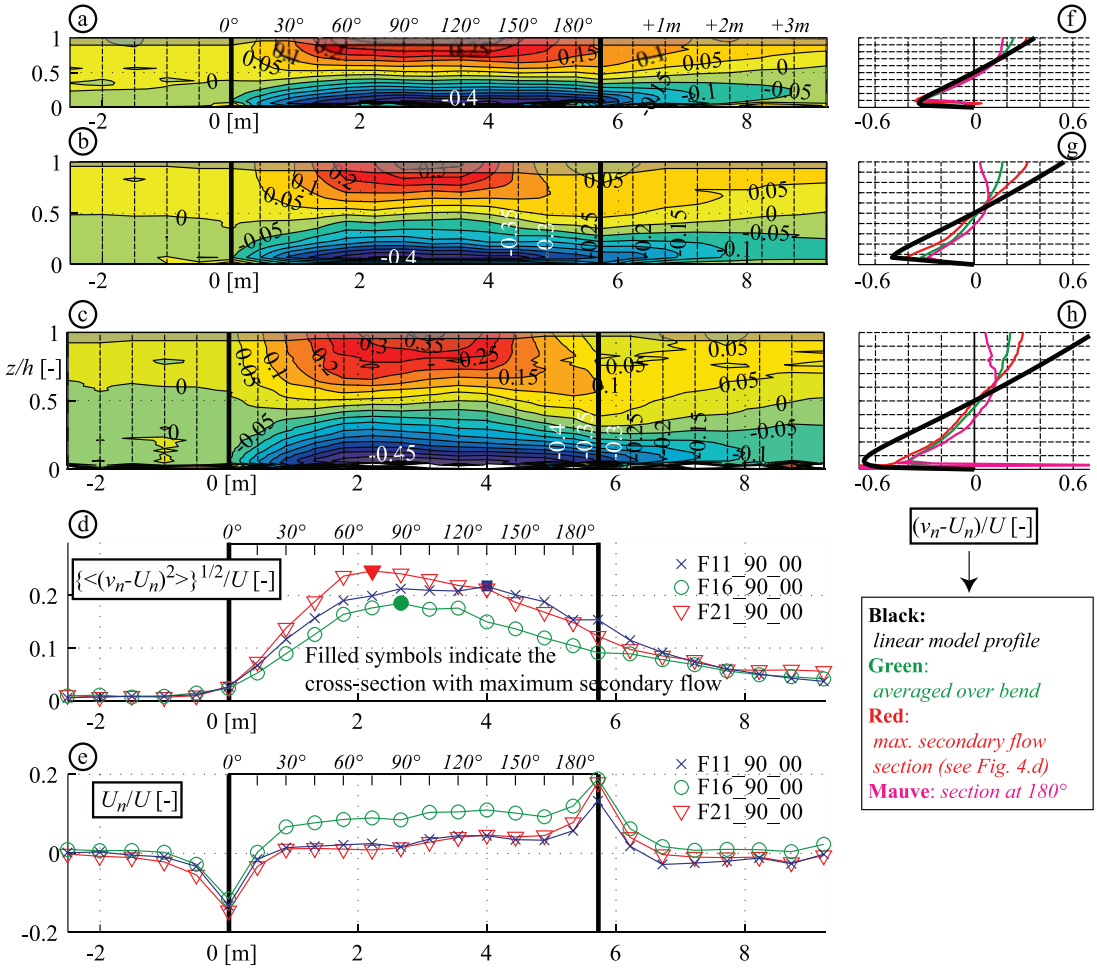

Figure 4. Isolines of the normalized circulatory part of the transverse velocity, $(v_n - U_n)/U$, along the centerline in (a) the F11_90_00 experiment, (b) the F16_90_00 experiment, and (c) the F21_90_00 experiment. Measured data have been extrapolated in the shaded near-surface region. Figures 4a–4c are distorted by a factor 10. (d) Streamwise distribution along the centerline of the normalized strength of the secondary flow, $\sqrt{\langle (v_n - U_n)^2 \rangle}/U$. (e) Streamwise distribution along the centerline of the normalized depth-averaged transverse velocity, U_n/U. (f–h) Circulatory part of the transverse velocity, $(v_n - U_n)/U$, according to the indicated legend in the F11_90_00, F16_90_00, and F21_90_00 experiments, respectively.

with maximum outward/inward transverse velocities near the water surface/bed as high as about 40% of the streamwise velocity. Remarkably, values at the bend exit are reduced to about half of these maximum values, which is mainly due to a pronounced decrease in the upper part of the water column. The cross section of maximum secondary flow is located at 135°, 90° and 75° in the bend for the F11_90_00, F16_90_00 and F21_90_00 experiments, respectively, which suggests that its location depends on the flow depth and is related to the aspect ratio B/H.

[37] Owing to mass conservation, the translatory cross flow U_n (Figure 4e) is strongly related to the transverse redistribution of streamwise velocity U_s around the bend. *Blanckaert and de Vriend* [2003, Figure 7] have illustrated the redistribution of streamwise velocity U_s around the bend by means of the parameter $(\alpha_s + 1)$, which is defined as

$$(\alpha_s + 1) = [(\partial U_s/\partial n)/(U_s/R) + 1] \quad (3)$$

It parameterizes the deviation of the $U_s(n)$ distribution from a potential vortex distribution. *Blanckaert and de Vriend* [2003] estimated α_s from detailed velocity measurements in various cross sections around the flume for the here reported experiments. Just downstream of the bend entry, $(\alpha_s + 1) \approx 0$, which implies that U_s decays from the inner bank toward the outer bank. Such an inward velocity redistribution is consistent with the observed strong inward cross flow, $U_n/U(s) \approx -0.2$. Subsequently, the core of maximum U_s values gradually shifts outward, as parameterized by a gradual increase of $(\alpha_s + 1)$. Such an outward velocity redistribution is consistent with the observed cross flow in the bend of $U_n/U \approx 0.05$. Near the bend exit, $(\alpha_s + 1)$ strongly increases to about 2, which corresponds to a free vortex distribution. Such a strong increase in $(\alpha_s + 1)$ is consistent with the observed pronounced outward cross flow $U_n/U \approx 0.2$. Cross flow is negligible in the straight outflow reach. The pronounced cross flow occurring near the bend entry

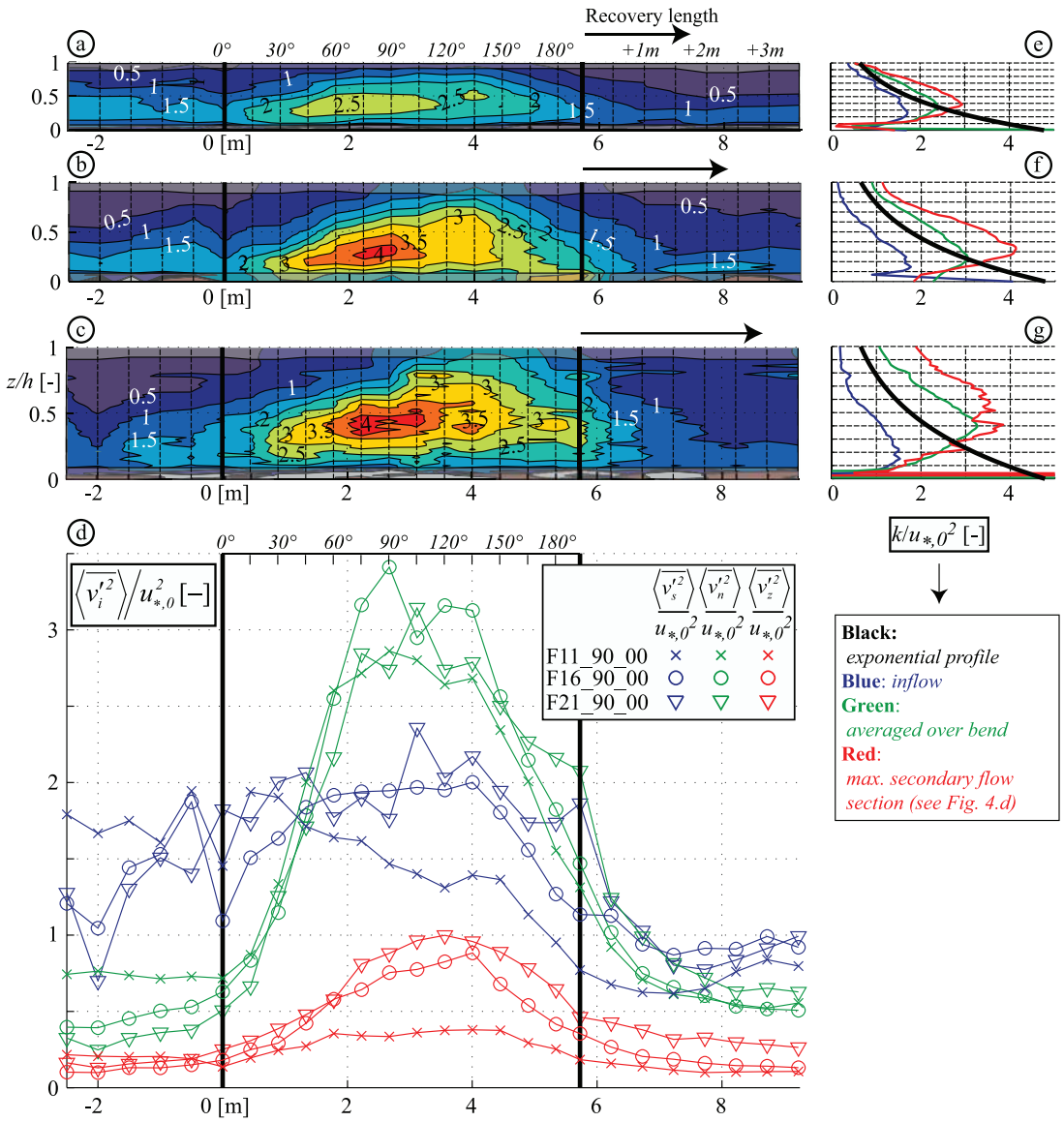

Figure 5. Isolines of the normalized turbulent kinetic energy, $k/u_{*,0}^2$, along the centerline in (a) the F11_90_00 experiment, (b) the F16_90_00 experiment, and (c) the F21_90_00 experiment. Measured data have been extrapolated in the shaded near-surface region and are inaccurate in the shaded near-bed region. Figures 5a–5c are distorted by a factor 10. (d) Streamwise distribution along the centerline of the normalized depth-averaged turbulent normal stresses, ($\langle \overline{v_s'^2} \rangle$, $\langle \overline{v_n'^2} \rangle$, $\langle \overline{v_z'^2} \rangle$)/$u_{*,0}^2$, in the three experiments. (e–g) Vertical profiles of the normalized turbulent kinetic energy, $k/u_{*,0}^2$, according to the indicated legend in the F11_90_00, F16_90_00, and F21_90_00 experiments, respectively.

and exit are due to the discontinuities in curvature and are therefore not representative of natural river bends.

3.3. Turbulence Characteristics Along the Centerline

[38] Figure 5 illustrates the evolution of the turbulent kinetic energy (*tke*) (Figures 5a–5c and 5e–5g) and the depth-averaged turbulent normal stresses (Figure 5d) along the centerline in the three experiments. Profiles in the straight inflow deviate considerably from the exponential profile proposed by *Nezu and Nakagawa* [1993] (Figures 5e–5g), which can be attributed to (1) the slightly accelerating flow in the straight inflow reach, which implies lower turbulence activity than in straight uniform flow [*Graf and Altinakar*, 1998], (2) the reduced accuracy of the ADVP in turbulence measurements near the bed due to large velocity gradients in the measuring volume, (3) the uncertainty in the estimation of the shear velocity which is used as normalization factor, and (4) the systematic underestimation of the vertical fluctuations. In spite of the experimental uncertainty, the measured patterns clearly indicate some relevant curvature-induced processes.

[39] The *tke* strongly increases upon entering the bend. Just below middle depth, a core of high *tke* is observed with maximum values between the cross sections at 75° and 105° that are about four times higher than in the straight inflow. In the second part of the bend, this core of high *tke* weakens and is reduced to about half of its maximum value at the bend exit. In the straight outflow reach, the *tke* distribution

Table 3. Summary of Normalized Depth-Averaged Turbulent Kinetic Energy and Turbulent Normal Stresses[a]

Experiment	Straight (Inflow + Outflow)	Bend	Maximum in Bend	Bend/Straight	Maximum in Bend/Straight
F11_90_00	0.97	1.94	2.34	2.01	2.41
	1.08	1.46	1.94	1.36	1.81
	0.71	2.12	2.86	2.99	4.05
	0.15	0.30	0.38	1.99	2.48
F16_90_00	0.96	2.29	3.06	2.40	3.20
	1.12	1.73	2.00	1.55	1.78
	0.63	2.29	3.41	3.67	5.46
	0.17	0.57	0.88	3.39	5.31
F21_90_00	1.03	2.40	3.23	2.34	3.15
	1.08	1.93	2.36	1.79	2.19
	0.70	2.18	3.14	3.11	4.50
	0.28	0.70	1.00	2.53	3.63

[a] $\langle k \rangle / u_{*,0}^2$, turbulent kinetic energy; $\langle \overline{v_i'^2} \rangle / u_{*,0}^2$, turbulent normal stresses, ($i = s, n, z$) (Figure 5), respectively. Averaged values in the straight reaches and the bend, maximum values in the bend, ratio of averaged values and maximum values in the bend to averaged values in the straight reaches, respectively.

recovers toward its straight uniform flow pattern. The recovery length seems to increase with flow depth as indicated by the isoline patterns in Figures 5a–5c. Although the streamwise and vertical turbulent normal stresses increase considerably in the bend, the increase in *tke* is mainly due to the transverse turbulent normal stress (Figure 5d), which becomes the dominant turbulent normal stress in the bend reach.

[40] Table 3 summarizes the normalized depth-averaged turbulent kinetic energy, $\langle k \rangle / u_{*,0}^2$, and turbulent normal stresses, $\langle \overline{v_i'^2} \rangle / u_{*,0}^2$ ($i = s, n, z$) in the straight reaches and the bend. The maximum/averaged values of the *tke* and transverse turbulent normal stress in the bend are about 2.9 ± 0.5/2.2 ± 0.2 times and 4.7 ± 0.7/3.3 ± 0.4 times higher than in the straight inflow reach, respectively.

[41] Figure 6 illustrates the evolution around the bend of the normalized turbulent shear stress, $\overline{v_s' v_n'} / u_{*,0}^2$. This shear stress is zero in straight flow but of dominant order of magnitude in the bend. The patterns of this shear stress show a core of high positive values in the first half of the bend, followed by a less pronounced core of negative values in the second half. Local extrema in these cores seem to increase slightly with the curvature ratio $\tilde{H}/R$. When considering depth-averaged values (Figure 6d), however, the core of negative values is not discernable anymore and the evolution is similar in all three experiments. This shear stress decays to zero in the straight outflow reach.

[42] Figure 7 illustrates the evolution around the bend of the normalized turbulent shear stress, $\overline{v_s' v_z'} / u_{*,0}^2$. Profiles in

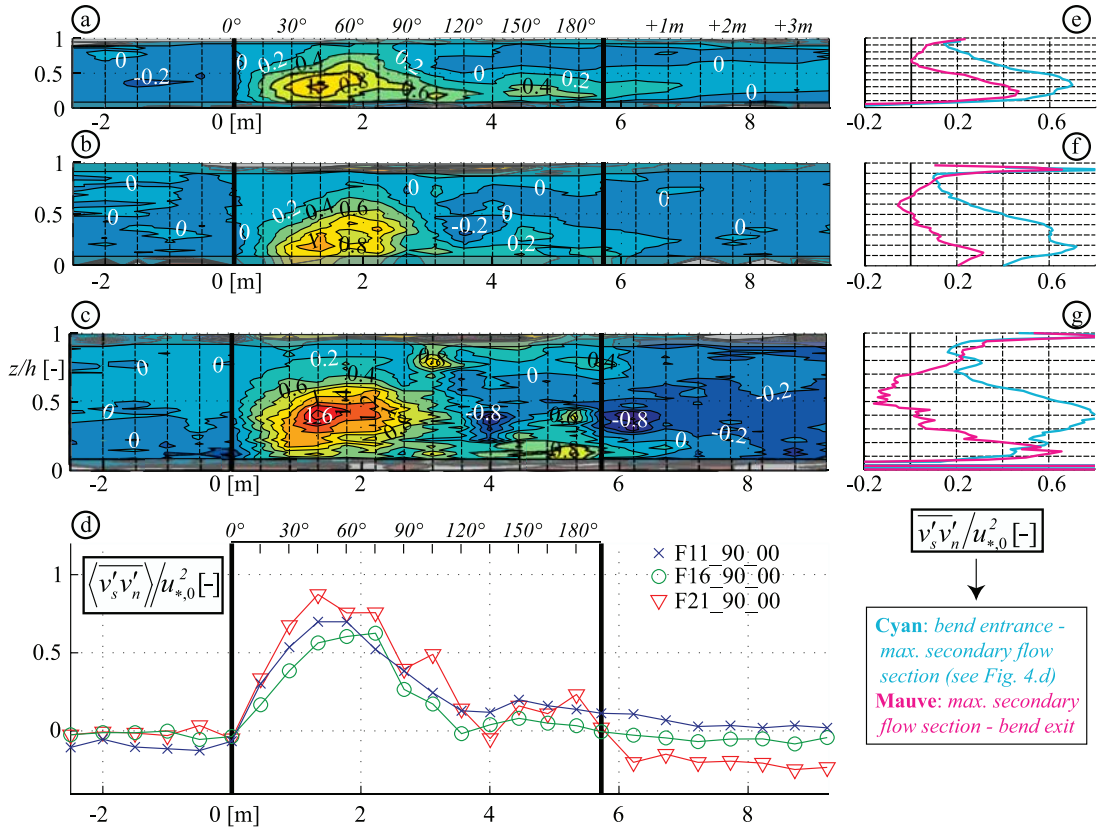

Figure 6. Isolines of the normalized turbulent shear stress, $\overline{v_s' v_n'} / u_{*,0}^2$, along the centerline in (a) the F11_90_00 experiment, (b) the F16_90_00 experiments, and (c) the F21_90_00 experiment. Measured data are inaccurate in the shaded regions near the water surface and the bed. Figures 6a–6c are distorted by a factor 10. (d) Streamwise distribution along the centerline of the depth-averaged normalized turbulent shear stress, $\overline{v_s' v_n'} / u_{*,0}^2$. (e–g) Vertical profiles of the normalized turbulent shear stress, $\overline{v_s' v_n'} / u_{*,0}^2$, according to the indicated legend in the F11_90_00, F16_90_00, and 21_90_00 experiments, respectively.

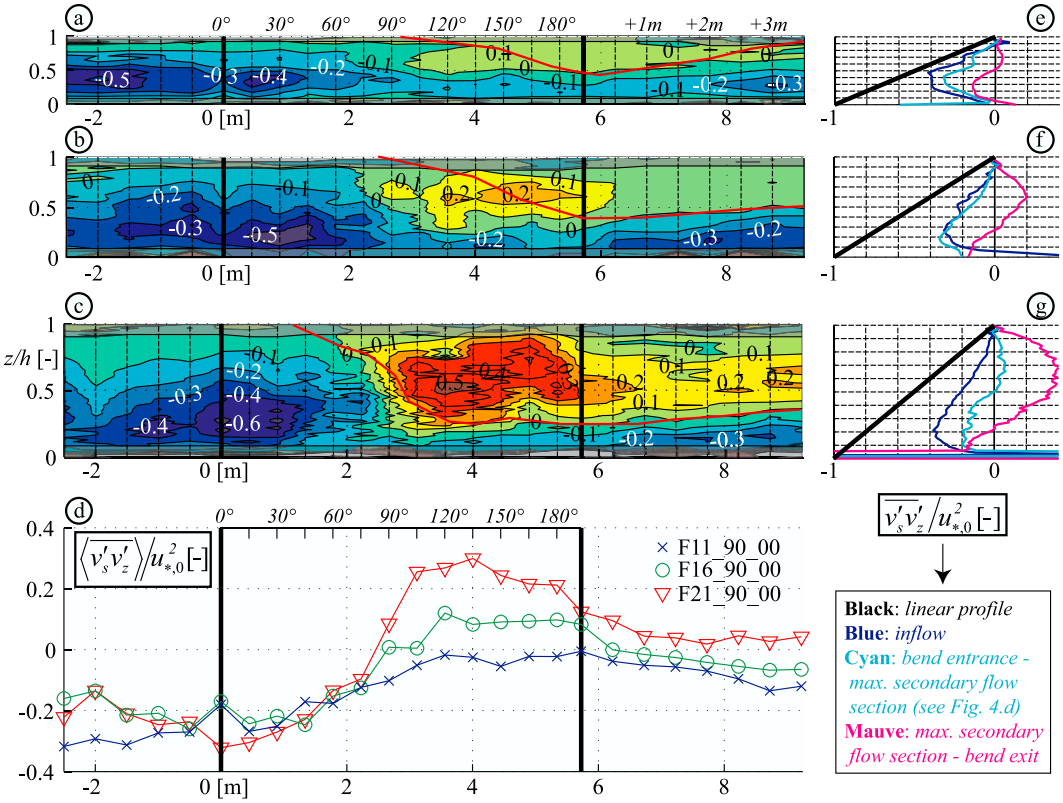

Figure 7. Isolines of the normalized turbulent shear stress, $\overline{v_s'v_z'}/u_{*,0}^2$, along the centerline in (a) the F11_90_00 experiment, (b) the F16_ 90_00 experiment, and (c) the F21_90_00 experiment. The red line indicates approximately the location where $\partial v_s/\partial z = 0$ (Figure 3). Measured data are inaccurate in the shaded regions near the water surface and the bed. Figures 7a–7c are distorted by a factor 10. (d) Streamwise distribution along the centerline of the depth-averaged normalized turbulent shear stress, $\langle\overline{v_s'v_z'}\rangle/u_{*,0}^2$. (e–g) Vertical profiles of the normalized turbulent shear stress, $\overline{v_s'v_z'}/u_{*,0}^2$, according to the indicated legend in the F11_90_00, F16_90_00, and 21_90_00 experiments, respectively.

the straight inflow deviate considerably from the theoretical linear profile in the straight inflow reach (Figures 6e–6g), which can be attributed to the same factors as for the *tke*. In spite of the uncertainty in the experimental data, the measured patterns clearly indicate some relevant curvature-induced processes.

[43] In the first part of the bend upstream of the cross section at 60°, only weak changes in the $\overline{v_s'v_z'}/u_{*,0}^2$ profiles are observed. In the second part of the bend, a core of positive $\overline{v_s'v_z'}/u_{*,0}^2$ values which are of dominant order of magnitude is observed in the upper part of the water column, whereas negative values seem to be concentrated in the near-bed region. The recovery toward straight flow profiles in the straight outflow reach is not yet accomplished at the flume's exit.

[44] The region with positive $\overline{v_s'v_z'}/u_{*,0}^2$ values corresponds rather well with the region where $\partial v_s/\partial z < 0$ (indicated in Figures 7a–7c based on Figure 3). The core of positive values seems to increase in size and magnitude with increasing curvature ratio $\tilde{H}/R$.

[45] Figure 8 illustrates the evolution around the bend of the normalized turbulent shear stress, $\overline{v_n'v_z'}/u_{*,0}^2$. This shear stress is zero in straight flow but of dominant order of magnitude in the bend. The behavior of this turbulent shear stress seems to be strongly related to the secondary flow (Figure 4): it increases in the first half of the bend, reaches a maximum value and decays rather strongly in the second half of the bend. Maximum values in the bend seem to increase with the curvature ratio $\tilde{H}/R$. The decay of this shear stress in the straight outflow seems to be considerably faster than that of other turbulent quantities.

4. Data Interpretation and Analysis

[46] Curvature is found to have a dominant influence on the mean flow and turbulence characteristics in the reported experiments. It generates secondary flow, redistribution of streamwise velocity and an increase in turbulence.

[47] According to low-amplitude perturbation models, secondary flow and turbulence would be expected to increase linearly with the curvature ratio, $\tilde{H}/R$; therefore they are called "linear models." The most remarkable feature of the reported experiments is that secondary flow and turbulent normal stresses are of very similar magnitude, whereas turbulent shear stresses only slightly increase in the three experiments, despite the pronounced different $\tilde{H}/R$ values. The mechanism underlying these observations will be analyzed hereafter.

4.1. Streamwise Velocity and Secondary Flow

[48] Various linear models for the secondary flow have been proposed in the literature [e.g., *van Bendegom*, 1947;

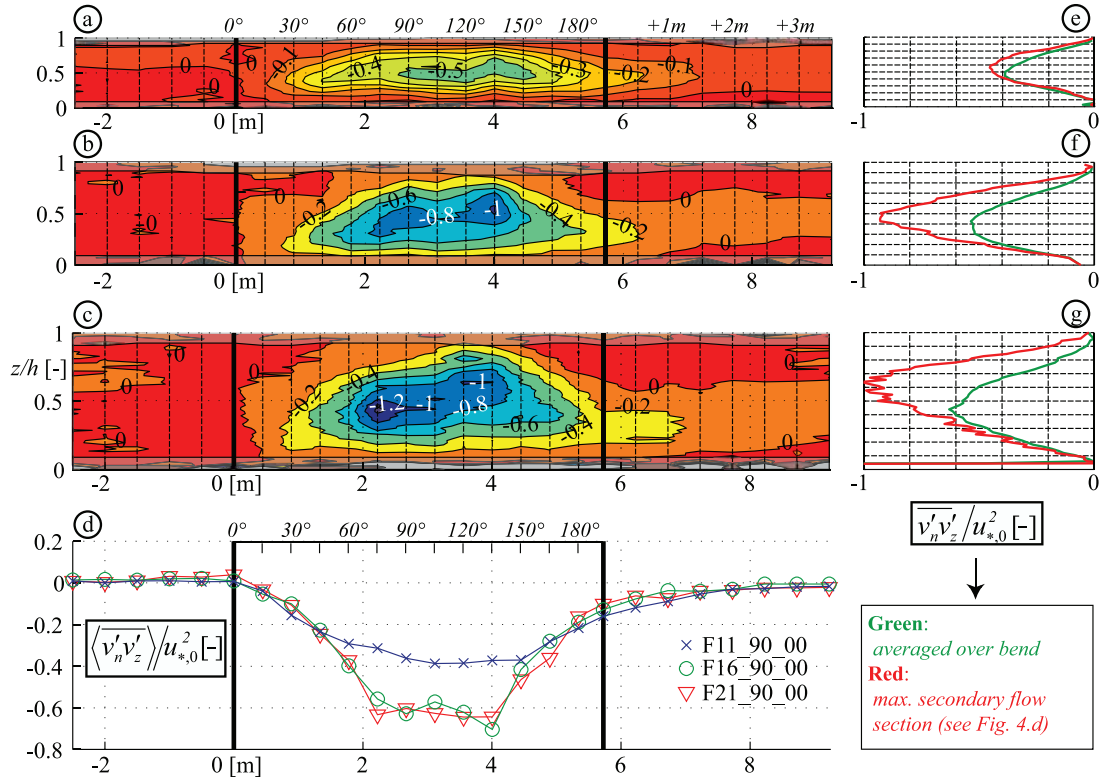

Figure 8. Isolines of the normalized turbulent shear stress, $\overline{v_n'v_z'}/u_{*,0}^2$, along the centerline in (a) the F11_90_00 experiment, (b) the F16_90_00 experiment, and (c) the F21_90_00 experiment. Measured data are inaccurate in the shaded regions near the water surface and the bed. Figures 8a–8c are distorted by a factor 10. (d) Streamwise distribution along the centerline of the depth-averaged normalized turbulent shear stress, $\langle\overline{v_n'v_z'}\rangle/u_{*,0}^2$. (e–g) Vertical profiles of the normalized turbulent shear stress, $\overline{v_n'v_z'}/u_{*,0}^2$, according to the indicated legend in the F11_90_00, F16_90_00, and 21_90_00 experiments, respectively.

Rozovskii, 1957; *Engelund*, 1974; *Kikkawa et al.*, 1976; *de Vriend*, 1977; *Odgaard*, 1986; *Johannesson and Parker*, 1989a]. They mainly differ in the choice of the eddy viscosity profile. Figures 4f–4h show that the profile of $(v_n - U_n)/U$ according to the model proposed by *de Vriend* [1977] considerably overestimates the secondary flow.

[49] On the basis of the analysis of advective momentum transport in open-channel bends [*Blanckaert and Graf*, 2004], *Blanckaert and de Vriend* [2003] have developed a nonlinear model for flow redistribution in open-channel bends that explains and quantifies the interaction between the profiles of streamwise velocity v_s and secondary flow $(v_n - U_n)$, including the observed saturation of secondary flow at high curvature. Their model and findings are briefly summarized hereafter.

[50] Advective transport of streamwise momentum by the secondary flow modifies the vertical v_s profile and thereby also the vertical gradient of the centrifugal force, $\partial(v_s^2/R)/\partial z$, which is the major driving force for the secondary flow. According to *Blanckaert and de Vriend*'s [2003] model, the profiles of v_s and $(v_n - U_n)$ depend on the dimensionless Chézy coefficient C_f and on a bend parameter which they define as

$$\beta = C_f^{-0.275}(H/R)^{-0.5}(\alpha_s + 1)^{0.25} \quad (4)$$

The interaction between v_s and $(v_n - U_n)$ is negligible when $\beta = 0$ but intensifies with increasing values of β. The $(\alpha_s + 1)$ contribution (equation (3)) in the definition of β is of particular importance since it accounts for the interaction between the horizontal distribution of the flow (U_s) and the vertical structure of the flow (v_s and $(v_n - U_n)$).

[51] The evolution of $(\alpha_s + 1)$ along the centerline in the reported experiments has been illustrated by *Blanckaert and de Vriend* [2003, Figure 7] as described in section 3.2. Just downstream of the bend entry, $(\alpha_s + 1) \approx 0$, which indicates a negligible interaction between v_s and $(v_n - U_n)$ implying that the v_s profiles remain close to logarithmic and $(v_n - U_n)$ tends to grow toward the values predicted by linear models. The parameter $(\alpha_s + 1)$ progressively increases around the bend, leading to the observed deformation of the v_s profile and decrease of secondary flow in the second part of the bend. The occurrence of the maximum secondary flow strength in the middle of the bend, well downstream of the cross section where $(\alpha_s + 1)$ and β are minimal is due to inertia. *Blanckaert and de Vriend* [2003] describe in detail the interaction between v_s and $(v_n - U_n)$ in the here reported experiments, which explains the saturation of the secondary flow.

4.2. Turbulence

[52] A spectral analysis of the turbulent fluctuations gives clues on the mechanisms underlying the curvature-induced

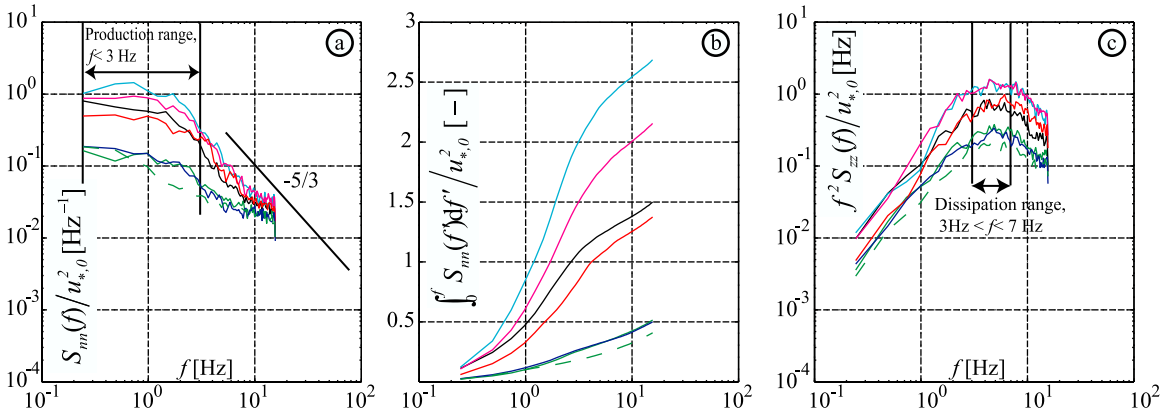

Figure 9. (a) Normalized power spectra of the transverse velocity fluctuations $S_{nn}(f)/u_{*,0}^2$ (Hz^{-1}); (b) normalized cumulative power spectra of the transverse velocity fluctuations $\int_0^f S_{nn}(f')df'/u_{*,0}^2$; (c) dissipation spectra based on the vertical velocity fluctuation $f^2S_{zz}(f)/u_{*,0}^2$ (Hz). Spectra are computed in the F16_90_00 experiment on the centerline at the bend entry (green), 45° (black), 90° (cyan), 135° (mauve), 180° (red) in the bend, 1.5 m (blue), and 3.5 m (green dashed) downstream of the bend exit. In order to reduce scatter, the computed spectra have been averaged over the water depth, excluding the near-bed ($z/h < 0.25$) and near-surface zones ($z/h > 0.75$) where the accuracy is reduced.

increase in *tke* and turbulent normal stresses (Figure 5). Figures 9a and 9b show normalized power spectra $S_{nn}(f)/u_{*,0}^2$ and normalized cumulative power spectra $\int_0^f S_{nn}(f')df'/u_{*,0}^2$ of the transverse velocity fluctuation in the F16_90_00 experiment, respectively, whereas Figure 9c shows dissipation spectra $f^2S_{zz}(f)/u_{*,0}^2$ [*Nezu and Nakagawa*, 1993]; f indicates the frequency in Hz. Since dissipation is dominant in the quasi-isotropic high-frequency domain, the dissipation spectra have been estimated from the vertical velocity fluctuations which are characterized by a lower parasitical noise level than the streamwise and transverse fluctuations [*Blanckaert and Lemmin*, 2006]. In order to reduce scatter, the computed spectra have been averaged over the water depth, excluding the near bed ($z/h < 0.25$) and near surface zones ($z/h > 0.75$).

[53] Figures 9a and 9b show the characteristic −5/3 slope in log-log presentation in the inertial subrange of the power spectra and the typical S shape of the cumulative power spectra [*Blanckaert and Lemmin*, 2006], although some contamination by parasitical noise occurs in the high frequency range, $f > 7$ Hz.

[54] The inertial subrange seems to be situated in the frequency range $f > 2$ Hz. The increase in transverse turbulent normal stresses mainly occurs in the low frequency range $f < 3$ Hz, which corresponds to the production range of turbulence. Differences between the spectra in the different cross sections are reduced in the high frequency range. Figure 9c indicates that dissipation also increases considerably in the bend with respect to straight flow. The maximum dissipation seems to occur in the frequency range 3 Hz $< f <$ 7 Hz, whereas the contribution of the frequency range $f <$ 3 Hz seems to be negligible. Figure 10 compares the evolution around the flume of the average values of the spectra of the transversal velocity fluctuations in the production range $f < 3$ Hz (Figure 9a) and the average values of the dissipation spectra in the range 3 Hz $< f <$ 7 Hz (Figure 9c) in the F11_90_00, F16_90_00 and F21_90_00 experiments. In general, the dissipation variable seems to lag behind the production variable and its variations seem to be attenuated; especially the increase in the first part of the bend seems to be less pronounced.

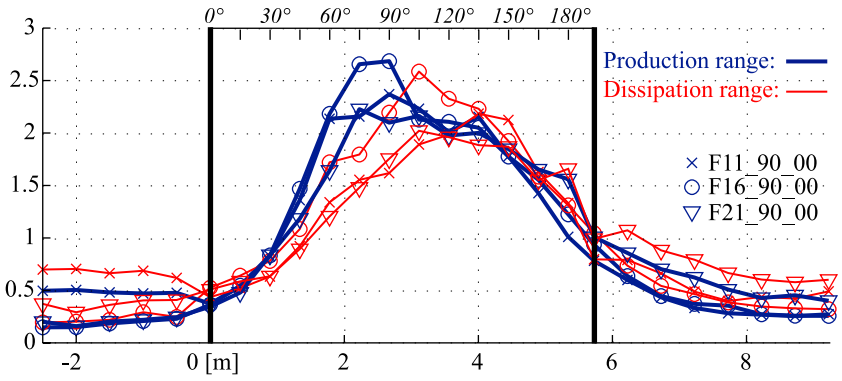

Figure 10. Streamwise distribution of the average values of the spectra of the transversal velocity fluctuations in the production range $f < 3$ Hz (Figure 9a) and the average values of the dissipation spectra in the range 3 Hz $< f <$ 7 Hz in the F11_90_00, F16_90_00, and F21_90_00 experiments. Values have been normalized such that the flume-averaged value equals 1.

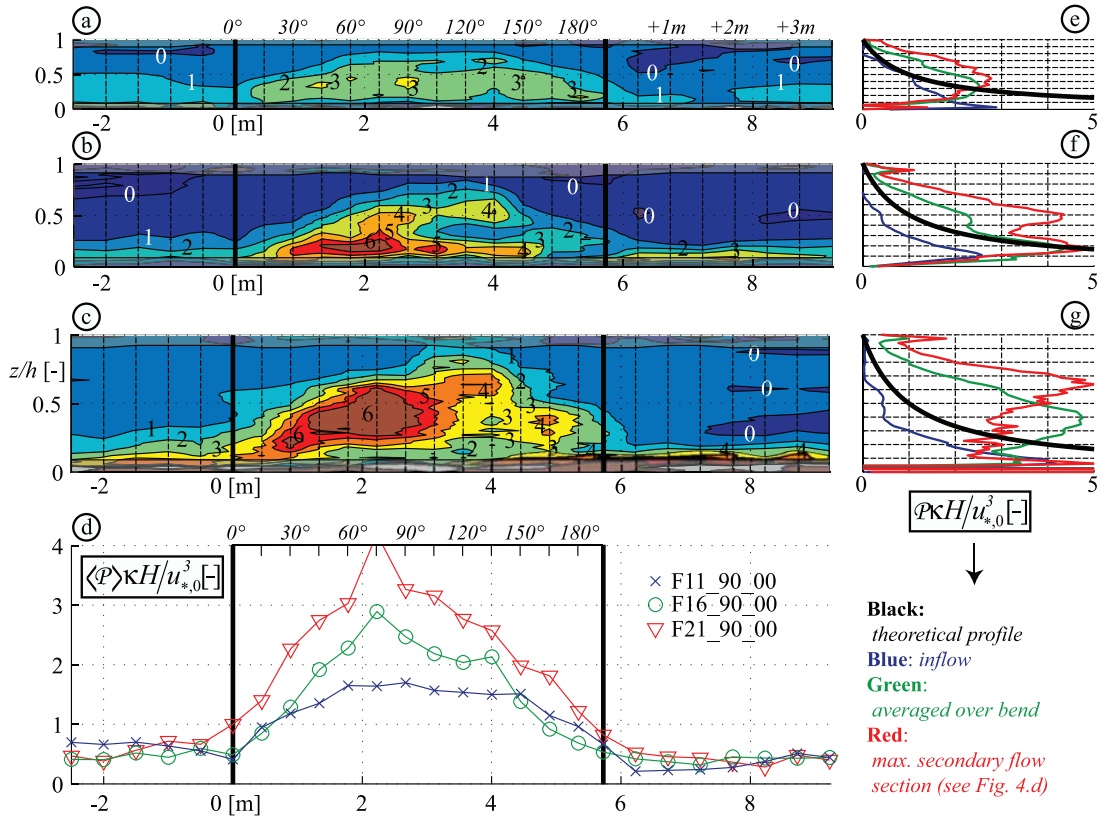

Figure 11. Isolines of the normalized turbulence production rate, $\mathcal{P}\ \kappa H/u_{*,0}^3$, along the centerline in (a) the F11_90_00 experiment, (b) the F16_90_00 experiment, and (c) the F21_90_00 experiment. Measured data are inaccurate in the shaded regions near the water surface and the bed. Figures 11a–11c are distorted by a factor 10. (d) Streamwise distribution along the centerline of the depth-averaged normalized turbulent production rate, $\langle\mathcal{P}\rangle\ \kappa H/u_{*,0}^3$, excluding the range $z/h < 0.1$. (e–g) Vertical profiles of the normalized turbulence production rate, $\mathcal{P}\ \kappa H/u_{*,0}^3$, according to the indicated legend in the F11_90_00, F16_90_00, and 21_90_00 experiments, respectively.

[55] These observations are in agreement with the energy cascade concept of turbulence: *tke* is generated in the low frequency range through the interaction between the time-averaged flow and large turbulent structures. While being advected in streamwise direction by the flow, these large turbulent structures disintegrate in smaller structures accompanied by an increase in frequency and in dissipation rate. On the basis of these observations, the further analysis of the mechanisms underlying the increased *tke* and turbulent normal stresses (Figure 5) will consider the evolution around the flume of the turbulence production rate (Figure 11) and the turbulence dissipation rate (Figure 12). The turbulence production rate is defined by [*Hinze*, 1975, chap. 1–13]

$$\mathcal{P} = -\left[\left(\overline{v_s'^2} - \frac{2}{3}k\right)e_{ss} + \left(\overline{v_n'^2} - \frac{2}{3}k\right)e_{nn} + \left(\overline{v_z'^2} - \frac{2}{3}k\right)e_{zz} + 2\overline{v_s'v_n'}e_{sn} + 2\overline{v_s'v_z'}e_{sz} + 2\overline{v_n'v_z'}e_{nz}\right] \tag{5}$$

$$\mathcal{P} = \mathcal{P}_{ss} + \mathcal{P}_{nn} + \mathcal{P}_{zz} + \mathcal{P}_{sn} + \mathcal{P}_{sz} + \mathcal{P}_{nz} \tag{6}$$

The definition of the strain rates, e_{jk} ($j, k = s, n, z$), according to *Batchelor* [1967, p. 600] and the applied estimation based on the measured data are given by

$$\left.\begin{aligned} e_{ss} &= \frac{1}{1+n/R}\frac{\partial v_s}{\partial s} + \frac{1}{1+n/R}\frac{v_n}{R} \approx \frac{\partial v_s}{\partial s} + \frac{v_n}{R} \\ e_{nn} &= \frac{\partial v_n}{\partial n} \approx 0 \\ e_{zz} &= \frac{\partial v_z}{\partial z} \approx 0 \\ e_{sn} &= \frac{1}{2}\left(\frac{1}{1+n/R}\frac{\partial v_n}{\partial s} + \frac{\partial v_s}{\partial n} - \frac{1}{1+n/R}\frac{v_s}{R}\right) \approx \frac{1}{2}\left(\frac{\partial v_n}{\partial s} + \alpha_s\frac{v_s}{R} - \frac{v_s}{R}\right) \\ e_{sz} &= \frac{1}{2}\left(\frac{1}{1+n/R}\frac{\partial v_z}{\partial s} + \frac{\partial v_s}{\partial z}\right) \approx \frac{1}{2}\left(\frac{\partial v_z}{\partial s} + \frac{\partial v_s}{\partial z}\right) \\ e_{nz} &= \frac{1}{2}\left(\frac{\partial v_z}{\partial n} + \frac{\partial v_n}{\partial z}\right) \approx \frac{1}{2}\frac{\partial v_n}{\partial z} \end{aligned}\right\} \tag{7}$$

[56] The applied estimations are based on the hypotheses that (1) the centerline is close the center of the secondary flow cell which guarantees that $e_{nn} \approx 0$ and $e_{zz} \approx 0$, (2) $\partial v_s/\partial n = \alpha_s(v_s/R)$ according to equation (3). The derivatives of the measured velocity patterns have been computed according to the procedure reported by Blanckaert (submitted manuscript, 2009).

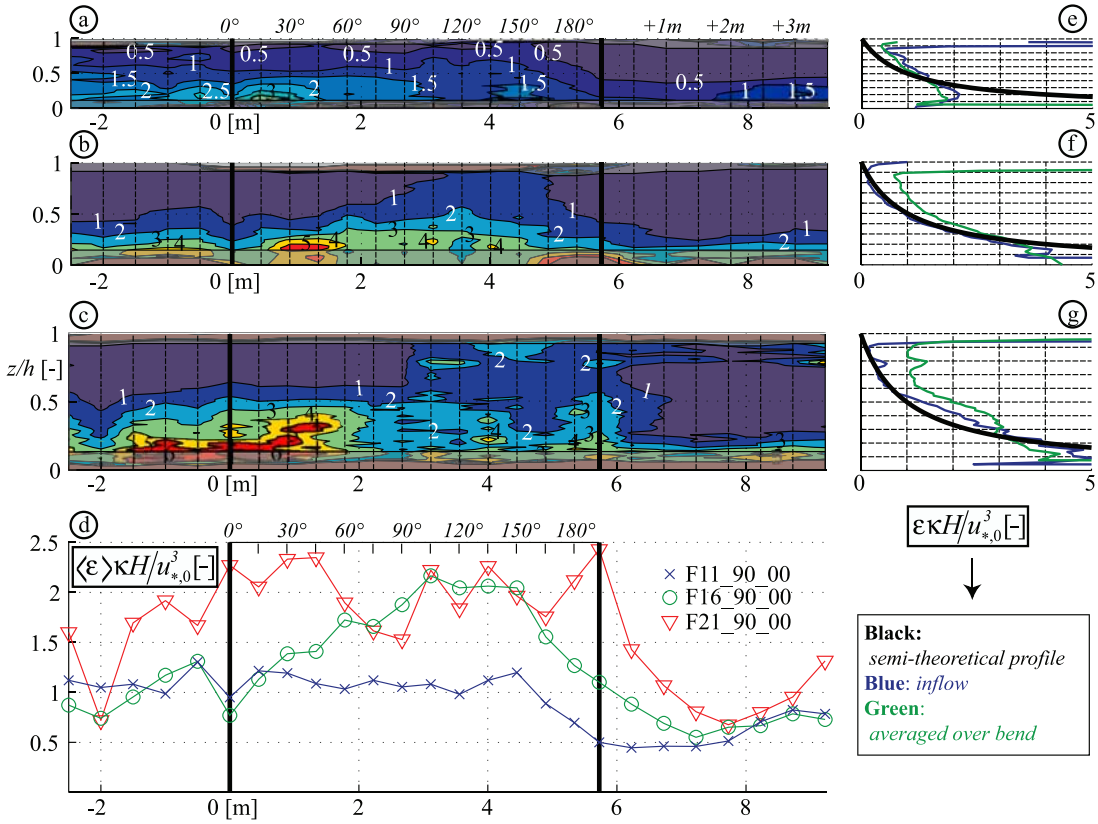

Figure 12. Isolines of the normalized turbulent dissipation rate, $\varepsilon\kappa H/u_{*,0}^3$, along the centerline in (a) the F11_90_00 experiment, (b) the F16_90_00 experiment, and (c) the F21_90_00 experiment. Measured data are inaccurate in the shaded regions near the water surface and the bed. Figures 12a–12c are distorted by a factor 10. (d) Streamwise distribution along the centerline of the depth-averaged normalized turbulent dissipation rate, $\langle\varepsilon\rangle\kappa H/u_{*,0}^3$, excluding the shaded regions. (e–g) Vertical profiles of the normalized turbulent dissipation rate, $\varepsilon\kappa H/u_{*,0}^3$, according to the indicated legend in the F11_90_00, F16_90_00, and 21_90_00 experiments, respectively.

[57] Agreement with theoretical profiles [*Nezu and Nakagawa*, 1993] in the straight inflow is satisfactorily (Figures 11e–11g). The accuracy is reduced in the lower part of the water column, $z/h < 0.2$. The systematic underestimation of the measured profiles may be attributed to the same factors as for *tke* (Figure 5) and $\overline{v_s' v_z'} u_{*,0}^2$ (Figure 7).

[58] The production rate of turbulence strongly increases upon entering the bend. At about middle depth, a core of high $\mathcal{P}$ is observed with maximum values between the cross sections at 45° and 105° that are about four times higher than in the straight inflow. In the second part of the bend, this core of high $\mathcal{P}$ weakens and is reduced to less than half of its maximum value at the bend exit. In the straight outflow reach, the $\mathcal{P}$ distribution recovers rather quickly toward its straight uniform flow pattern. The maximum values of $\mathcal{P}$ in the bend seem to increase with the curvature ratio $\tilde{H}/R$.

[59] The turbulent dissipation rate ε is estimated from the inertial subrange in the energy spectrum according to the procedure given by *Nezu and Nakagawa* [1993, section 4.6]. Profiles in the straight inflow reach agree surprisingly well with the theoretical profiles [*Nezu and Nakagawa*, 1993], given the relatively high uncertainty in the estimates of ε.

[60] Turbulent dissipation seems to be higher in the bend than in the straight reaches, although this tendency is less clear in the straight inflow reach. Just downstream of the bend entry, a core of higher values is discernable in the lower half of the flow depth. When considering depth-averaged values, however, the increase of dissipation seems to be rather uniform over the entire bend. The dissipation rate seems to increase with the curvature ratio $\tilde{H}/R$.

[61] As suggested by the spectral analysis (Figures 9 and 10), differences between the patterns of turbulence production and dissipation may explain the observed increase in *tke* and turbulent normal stresses in the bend (Figure 5). Table 4 summarizes normalized turbulence production and

Table 4. Summary of Normalized Turbulence Production and Dissipation Rates Averaged Over the Inflow Reach, Bend Reach, Outflow Reach, and Bend Plus Outflow Reach[a]

Experiment	Inflow	Bend	Outflow	Bend + Outflow
F11_90_00	0.54	1.26	0.44	0.95
	1.08	1.03	0.58	0.86
F16_90_00	0.42	1.62	0.47	1.18
	0.99	1.64	0.73	1.29
F21_90_00	0.53	2.39	0.47	1.66
	1.49	2.02	1.09	1.67

[a] $\mathcal{P}\kappa H/u_{*,0}^3$, turbulence production rate (Figure 9); $\varepsilon\ \kappa H/u_{*,0}^3$, turbulence dissipation rate (Figure 10).

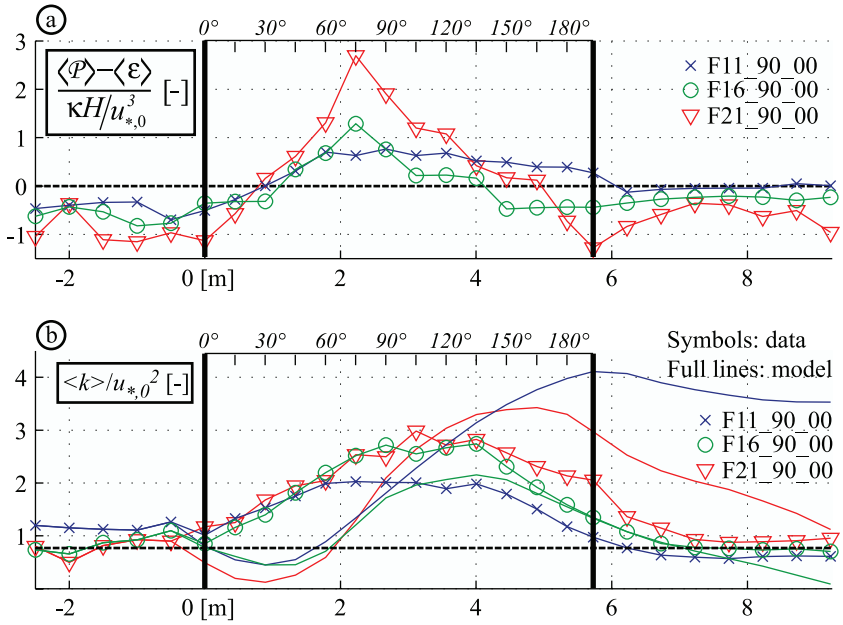

Figure 13. (a) Streamwise distribution along the centerline of the depth-averaged normalized turbulent production rate, $\langle \mathcal{P} \rangle \ \kappa H/u_{*,0}^3$ (Figure 11d), minus the depth-averaged normalized turbulent dissipation rate, $\langle \varepsilon \rangle \kappa H/u_{*,0}^3$ (Figure 12d), in the F11_90_00, F16_90_00, and 21_90_00 experiments. (b) Streamwise distribution of normalized depth-averaged turbulent kinetic energy, $\langle k \rangle / u_{*,0}^2$, from measurements (Figure 5) and computed according to equation (8) for the F11_90_00, F16_90_00, and 21_90_00 experiments.

dissipation rates, $\mathcal{P} \ \kappa H/u_{*,0}^3$ (Figure 11) and $\varepsilon \kappa H/u_{*,0}^3$ (Figure 12), respectively (κ = 0.4 is the von Karman constant), averaged over the inflow reach, bend reach, outflow reach and bend plus outflow reach. The experimental uncertainties in the turbulence production and dissipation rates are inherently high and have been estimated at 50% and 100%, respectively. Moreover, measurements of turbulence production and dissipation rates are systematically underestimated in the near bed region where these variables attain their highest values (Figures 11e–11g and Figures 12e–12g, respectively), leading to systematic underestimations of the averaged values reported in Table 4. These high experimental uncertainties and systematic errors make the following data interpretation unavoidably somewhat tentative:

[62] 1. Dissipation seems to be considerably overestimated in the straight inflow reach, where it should theoretically be equal to production. It is not clear if these deviations are uniquely due to the experimental uncertainty or if they have a physical basis.

[63] 2. When excluding the straight inflow reach, however, the total production and dissipation differ by less than 10% and can be considered in equilibrium.

[64] 3. Turbulence production seems to react faster to changes in curvature than turbulent dissipation: its growth is more pronounced in the first part of the bend, it reaches higher maximum values, and it recovers faster toward "straight flow" patterns in the straight outflow reach. The slower adaptation of the turbulent dissipation seems to attenuate spatial variations. This different behavior of the production and dissipation rate of *tke* is in agreement with the concept of the turbulent energy cascade as aforementioned in the spectral analysis.

[65] 4. Averaged over the bend, production seems to be higher than dissipation, which is compensated by the higher dissipation in the straight outflow reach.

[66] 5. The increase of *tke* and turbulent normal stresses can be attributed to these different spatial distributions of the turbulent production and dissipation. Turbulent production shows more spatial variation than dissipation and reaches considerably higher peak values. The regions where the peak values in production occur correspond rather well with the region of maximum *tke* and turbulent normal stresses.

[67] The relation between spatial differences in production and dissipation rate of turbulence at the one hand and the increase in *tke* at the other can be quantified by means of the transport equation for depth-averaged *tke* [*Hinze*, 1975] reduced to its three principal terms:

$$U \frac{\partial \langle k \rangle}{\partial s} = \langle \mathcal{P} \rangle - \langle \varepsilon \rangle \tag{8}$$

[68] Figure 13a shows the difference between $\langle \mathcal{P} \rangle$ and $\langle \varepsilon \rangle$ in all three experiments. It is positive in the first part of the bend, and negative toward the bend exit as well as in the straight outflow reach. It deviates from its theoretical zero value in the straight inflow. Figure 13b compares the measured distribution of $\langle k \rangle$ to the one obtained by integrating equation (8) based on the measured patterns of $\langle \mathcal{P} \rangle$ and $\langle \varepsilon \rangle$. The order of magnitude and patterns of the curvature-induced *tke* are satisfactorily reproduced by equation (8), given the high uncertainty in the result due experimental errors and error propagation. The large spatial lag between measured and modeled *tke* in Figure 13b arises

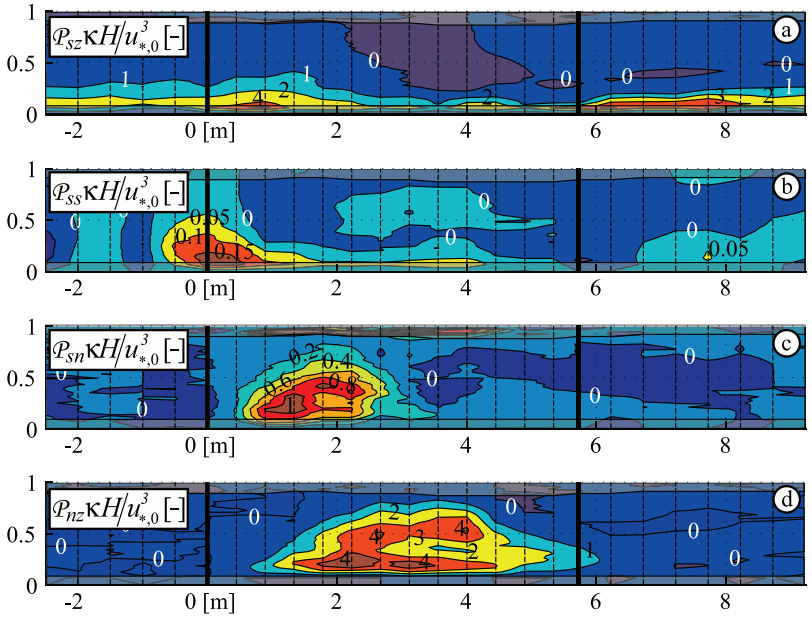

Figure 14. Isolines of the main contributions to the normalized turbulence production rate along the centerline in the F16_90_00 experiments: (a) $\mathcal{P}_{sz}\kappa H/u^3_{*,0}$, (b) $\mathcal{P}_{ss}\kappa H/u^3_{*,0}$, (c) $\mathcal{P}_{sn}\kappa H/u^3_{*,0}$, and (d) $\mathcal{P}_{nz}\kappa H/u^3_{*,0}$. The total normalized turbulence production rate along the centerline is estimated in Figure 11b. Measured data are inaccurate in the shaded regions near the water surface and the bed. Figures 14a–14c are distorted by a factor 10.

because the measured $\langle \mathcal{P} \rangle - \langle \varepsilon \rangle < 0$ in the beginning of the bend. Figure 14 investigates the mechanisms underlying the increase in turbulence production rate, by analyzing the dominant individual contributions according to equations (6) and (7).

[69] In straight uniform flow, $\mathcal{P}_{sz}$ (Figure 14a) is the only contribution to the turbulence production rate. Profiles of $\mathcal{P}_{sz}$ are slightly modified in the bend owing to the deformation of the v_s profiles (Figure 3), but $\mathcal{P}_{sz}$ remains of dominant magnitude all along the flume. $\mathcal{P}_{ss}$ (Figure 14b) is negligible except at the bend entrance. But the core of high values at the bend entrance can be attributed to the discontinuity in curvature and is therefore not representative for natural river configuration. A core of nonnegligible $\mathcal{P}_{sn}$ (Figure 14c) values, generated by the core of high turbulent shear stress $\overline{v'_s v'_n}/u^2_{*,0}$, exists in the bend reach between 30° and 75°. $\mathcal{P}_{nz}$ (Figure 14d) is the dominant curvature-induced contribution to turbulence production. Its close relation to the secondary flow through the strain rate $e_{nz} \approx \partial v_n/\partial z$ and the turbulence shear stress $\overline{v'_n v'_z}/u^2_{*,0}$ will be further investigated in section 5.

[70] According to *Hinze* [1975, p. 325], $\mathcal{P}_{nz}$ occurs in the production terms for the transverse turbulent normal stress $\overline{v'^2_n}$ while $\mathcal{P}_{ss}$, $\mathcal{P}_{sn}$ and $\mathcal{P}_{sz}$ occur in the production terms for the streamwise turbulent normal stress $\overline{v'^2_s}$. This explains why $\overline{v'^2_n}$ becomes the dominant turbulent stress in the bend reach (Figure 5d).

4.3. Energy Losses and Friction Coefficient

[71] Figure 2a has shown that energy losses, as quantified by the streamwise energy gradient, $E_s(s)$, increase by about 40% owing to curvature effects in all three experiments. On the basis of the hypothesis that the dimensionless Chézy coefficient C_f is constant in the cross section, E_s can be approximated as

$$E_s = \frac{\langle\langle |\vec{\tau}_b| \rangle\rangle}{\rho g R_h} = \frac{C_f \left\langle \left\langle |\vec{U}|^2 \right\rangle \right\rangle}{g R_h} \tag{9}$$

Where $\langle\langle\ \rangle\rangle$ represents cross-sectional averaged values and $|\vec{\tau}_b|$ the magnitude of the boundary shear stress vector. The observed increase of the energy gradient can be attributed to the following mechanism: (1) the additional transverse component of the boundary shear stress induced by the secondary flow, (2) the increased near-bed gradient of the velocity vector due to the deformed v_s profiles (Figure 3), (3) the nonuniform distribution of the depth-averaged velocity, which implies $\langle\langle |\vec{U}^2| \rangle\rangle > U^2$, and (4) the increased production rate of turbulence, which is by definition an increased loss of mean flow kinetic energy.

[72] *Blanckaert and de Vriend*'s [2003, Figure 10] nonlinear model for curved flow quantifies the first two mechanisms. It defines a correction factor to the friction coefficient $\psi_{\text{secondary flow}} = C_f/C_{f,0} = |\vec{\tau}_{\text{b,bend}}|/|\vec{\tau}_{\text{b,straight}}|$ as a function of the parameter $\beta C_f^{-0.15}$. On the basis of the experimental data, the average value of this factor ψ along the centerline in the bend is about

$$\left\{\psi_{\text{secondary flow}}\right\}_{\text{bend},n=0} = \left\{\frac{C_f}{C_{f,0}}\right\}_{\text{bend},n=0} = \left\{\frac{|\vec{\tau}_{b,\text{bend}}|}{|\vec{\tau}_{b,\text{straight}}|}\right\}_{\text{bend},n=0} \approx 1.2,\ 1.3 \text{ and } 1.4 \tag{10}$$

for the F11_90_00, F16_90_00 and F21_90_00 experiments, respectively. Since the secondary flow is maximum on the

centerline, the bend averaged value of $\psi_{\text{secondary flow}}$ is expected to be lower than the average value along the centerline.

[73] The relevance of the third mechanism can be estimated on the basis of a linearization of the velocity distribution according to equation (3): $U_{linear}(s, n) = U(s)(1 + \alpha_s(s)n/R)$. Averaging over the cross section (the average is in fact taken over a bend sector in order to take into account that arc length is longer/shorter in the outer/inner part of the cross section than on the centerline), gives

$$\psi_{\alpha_s} = \frac{\left\langle\left\langle |\vec{U}|^2 \right\rangle\right\rangle}{U^2} = 1 + \frac{1}{12}\left(\alpha_s^2 + 2\alpha_s\right)\frac{B^2}{R^2} \tag{11}$$

This effect can only cause a relevant increase in energy gradient of maximum 50% in very sharp bends where a mobile bed topography causes high α_s values. In the three reported experiments, however, the negative α_s values in a large part of the bend cause a negligible bend-averaged decrease in energy gradient.

[74] These observations suggest that the increased production rate of *tke* in the bend of O(100%) (Table 4) is a mechanism of dominant order of magnitude in the experiments. This mechanism will be further analyzed in section 5.

5. Modeling Implications

[75] As aforementioned, the nonlinear model of *Blanckaert and de Vriend* [2003] is able to explain the interaction between vertical profiles of the streamwise velocity v_s and the secondary flow, $(v_n - U_n)$. This section will focus on the modeling of the curvature-induced increase in *tke* and in energy losses.

[76] According to section 4, the spatial distribution of the production rate of turbulence $\mathcal{P}$ (Figure 11) is a dominant mechanism with respect to the curvature-induced increase in energy losses and *tke* (Figure 5). The model proposed hereafter for curvature-induced increase in energy losses and *tke* will be based on a model for the curvature-induced increase in turbulence production rate $\mathcal{P}$.

[77] The production rate of turbulence in straight uniform flow $\mathcal{P}_{\text{straight}}$ is theoretically known as [*Nezu and Nakagawa*, 1993]

$$\mathcal{P}_{\text{straight}} = \mathcal{P}_{\text{sz}} = -2\overline{v_s'v_z'}e_{sz} = 4\nu_t e_{sz}^2 = \frac{u_{*,0}^3}{\kappa h}\left(\frac{1 - z/h}{z/h}\right) \tag{12}$$

$\mathcal{P}_{\text{bend}}$ will be approximated on the basis of its major contributions as (equations (5), (6), (7))

$$\begin{aligned}\mathcal{P}_{\text{bend}} &\approx \mathcal{P}_{\text{ss}} + \mathcal{P}_{\text{sn}} + \mathcal{P}_{\text{sz}} + \mathcal{P}_{\text{nz}} \\ &= -\left[\left(\overline{v_s'^2} - \frac{2}{3}k\right)e_{ss} + 2\overline{v_s'v_n'}e_{sn} + 2\overline{v_s'v_z'}e_{sz} + 2\overline{v_n'v_z'}e_{nz}\right]\end{aligned} \tag{13}$$

The contribution $\mathcal{P}_{ss}$ is probably of minor importance but has been included for completeness. Modeling of the production rate requires modeling of the turbulent stresses. Figure 15 shows the patterns of the turbulent shear stresses for the F16_90_00 experiment estimated from the experimental strain rates according to the parabolic eddy viscosity model:

$$\left(\left[\overline{v_j'v'}_k\right]_{\nu_t} - \frac{2}{3}\delta_{jk}k\right) = -2\nu_t e_{jk} \tag{14}$$

$$\nu_t = \kappa u_{*,0} h\left[\frac{z}{h}\left(1 - \frac{z}{h}\right)\right] \tag{15}$$

[78] The Kronecker delta is indicated by the symbol δ_{jk} and ν_t is the eddy viscosity. The shear stress $\overline{v_n'v_z'}$ related to the secondary flow is particularly well reproduced by the eddy viscosity model. The eddy viscosity estimation of the shear stress $\overline{v_s'v_z'}$ reproduces satisfactorily the major features of the measured distribution. Contrary to the measured distribution (Figure 7b), it does not suffer from systematic underestimations of the vertical velocity fluctuations which are pronounced near the bed. The eddy viscosity estimation of $\overline{v_s'v_n'}$ is less accurate: the estimated core of positive values is too large and too weak. In general, however, the eddy viscosity estimations of the shear stresses are sufficiently accurate for modeling of the production rate of turbulence.

[79] On the basis of equations (13) and (14) and assuming that $\mathcal{P}_{sz,\text{bend}} \approx \mathcal{P}_{sz,\text{straight}}$ (Figure 14a) the production rate of turbulence in the bend can be modeled as

$$\mathcal{P}_{\text{bend}} \approx \mathcal{P}_{\text{straight}} + 2\nu_t\left[e_{ss}^2 + 2e_{sn}^2 + 2e_{nz}^2\right] \tag{16}$$

This can be further elaborated by approximating the strain rates (equation (7)) based on a linear approximation of the vertical profiles of $v_n = v_{n,surface}(2z/h - 1)$, where $v_{n,surface}$ is the transverse component of the secondary flow at the water surface, and an adaptation length $\lambda \sim H/C_f^{1/2}$ [*de Vriend*, 1981; *Johannesson and Parker*, 1989a] of the secondary flow into

$$\left.\begin{aligned} e_{ss} &\approx \frac{\partial v_s}{\partial s} + \frac{v_n}{R} \approx \frac{v_{n,surface}}{R}\left(2\frac{z}{h} - 1\right) \\ e_{sn} &\approx \frac{1}{2}\left(\frac{\partial v_n}{\partial s} + \alpha_s\frac{v_s}{R} - \frac{v_s}{R}\right) \approx \frac{1}{2}\left(\frac{v_{n,surface}}{\lambda}\left(2\frac{z}{h} - 1\right) + (\alpha_s - 1)\frac{U}{R}\right) \\ e_{nz} &\approx \frac{1}{2}\frac{\partial v_n}{\partial z} \approx \frac{v_{n,surface}}{h} \end{aligned}\right\} \tag{17}$$

$$\begin{aligned}\mathcal{P}_{\text{bend}} \approx \mathcal{P}_{\text{straight}} + 2\nu_t\Bigg[&\left(\frac{v_{n,surface}}{R}\right)^2\left(2\frac{z}{h} - 1\right)^2 \\ &+ \frac{1}{2}\left(\frac{v_{n,surface}}{\lambda}\left(2\frac{z}{h} - 1\right) + (\alpha_s - 1)\frac{U}{R}\right)^2 + 2\left(\frac{v_{n,surface}}{h}\right)^2\Bigg]\end{aligned} \tag{18}$$

Subsequently substituting equation (15) gives

$$\frac{\mathcal{P}_{\text{bend}}}{\mathcal{P}_{\text{straight}}} \approx 1 + \left[2\kappa^2\left(C_f^{-1/2}\frac{v_{n,surface}}{U}\right)^2\right]\left(\frac{z}{h}\right)^2\left\{\left(2\frac{z}{h} - 1\right)^2\left(\frac{h}{R}\right)^2 + \frac{1}{2}\left[C_f^{1/2}\left(2\frac{z}{h} - 1\right) + (\alpha_s - 1)\left(\frac{U}{v_{n,surface}}\frac{h}{R}\right)\right]^2 + 2\right\} \tag{19}$$

$$\frac{\mathcal{P}_{\text{bend}}}{\mathcal{P}_{\text{straight}}} \approx 1 + \left[2\kappa^2\left(C_f^{-1/2}\frac{v_{n,surface}}{U}\right)^2\right]\text{O}(1)\left\{\quad \text{O}\left(\left(\frac{h}{R}\right)^2\right) \quad + \quad \left(< \frac{1}{10}\right) \quad + 2\right\}$$

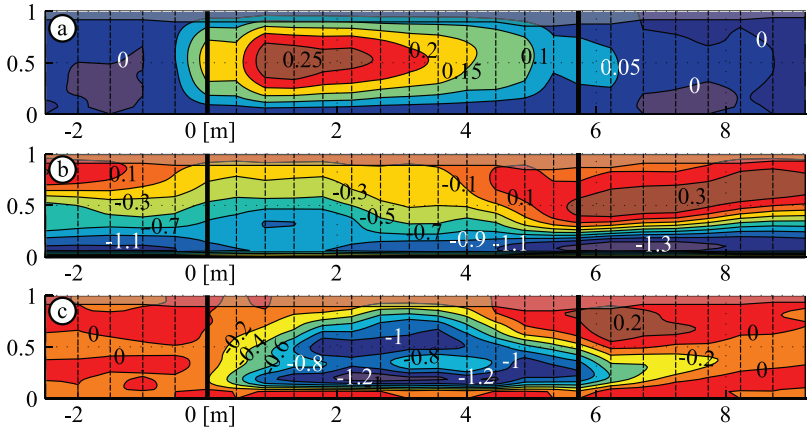

Figure 15. Isolines along the centerline of the normalized turbulent shear stresses in the F16_90_00 experiment estimated from the strain rates by means of a parabolic eddy viscosity: (a) $\lfloor \overline{v_s' v_n'} \rfloor \nu_t / u_{*,0}^2 = -2\nu_t e_{sn}/u_{*,0}^2$, (b) $\lfloor \overline{v_s' v_z'} \rfloor \nu_t / u_{*,0}^2 = -2\nu_t e_{sz}/u_{*,0}^2$, (c) $\lfloor \overline{v_n' v_z'} \rfloor \nu_t / u_{*,0}^2 = -2\nu_t e_{nz}/u_{*,0}^2$. The measured normalized turbulent shear stresses are shown in Figures 6b, 7b, and 8b. Measured data are inaccurate in the shaded regions near the water surface and the bed. Figures 15a–15c are distorted by a factor 10.

[80] Figure 16 shows the production rate $\mathcal{P}_{\text{bend}}$ as well as the dominant individual contributions $\mathcal{P}_{sn}$ and $\mathcal{P}_{nz}$ in the F16_90_00 experiment according to equation (19), where $v_{n,surf}$ has been estimated by fitting a linear profile to the measured pattern of $(v_n - U_n)$ (Figure 4) and α_s has been based on the experimental data [*Blanckaert and de Vriend*, 2003, Figure 7]. The total production rate of turbulence $\mathcal{P}_{\text{bend}}$ and the dominant curvature-induced contribution $\mathcal{P}_{nz}$ estimated according to this simplified model (equation (19)) agree surprisingly well with the experimental data (compare Figures 16a–16c to Figures 11b, 14c, and 14d, respectively). The modeled $\mathcal{P}_{sn}$ contribution shows the correct tendency but considerably underestimated the experimental values. This contribution is not of dominant order of magnitude, however. The $\mathcal{P}_{ss}$ contribution (not shown) is negligible.

[81] Depth averaging of equation (19) yields

$$\frac{\langle \mathcal{P}_{\text{bend}} \rangle}{\langle \mathcal{P}_{\text{straight}} \rangle} \approx 1 + \frac{\left[2\kappa^2 \left(C_f^{-1/2} \frac{v_{n,surface}}{U}\right)^2\right] \left\{ \left(\frac{h}{R}\right)^2 + \frac{1}{2}\left[\left(C_f^{1/2}\right)^2 + 5(\alpha_s - 1)^2 \left(\frac{U}{v_{n,surface}} \frac{h}{R}\right)^2\right] + 10 \right\}}{30\left\{ ln\left[\left(\frac{z_0}{h}\right)^{-1}\right] - \left(1 - \frac{z_0}{h}\right)\right\}}$$

$$\frac{\langle \mathcal{P}_{\text{bend}} \rangle}{\langle \mathcal{P}_{\text{straight}} \rangle} \approx 1 + \frac{\kappa^2}{10} \left(C_f^{-1/2} \frac{v_{n,surface}}{U}\right)^2 \frac{200}{30\left\{ ln\left[\left(\frac{z_0}{h}\right)^{-1}\right] - \left(1 - \frac{z_0}{h}\right)\right\}} \left\{ \frac{1}{10}\left(\frac{h}{R}\right)^2 + \frac{1}{20}\left[\left(C_f^{1/2}\right)^2 + 5(\alpha_s - 1)^2 \left(\frac{U}{v_{n,surface}} \frac{h}{R}\right)^2\right] + 1 \right\} \quad (20)$$

$$O(1) \qquad \left\{ O\left(\frac{1}{10}\left(\frac{h}{R}\right)^2\right) + O(10^{-3}) + O(10^{-1}) + 1 \right\}$$

$$\frac{\langle \mathcal{P}_{\text{bend}} \rangle}{\langle \mathcal{P}_{\text{straight}} \rangle} \approx 1 + \frac{\kappa^2}{10} \left(C_f^{-1/2} \frac{v_{n,surface}}{U}\right)^2 \quad (21)$$

Since the theoretical $\mathcal{P}$ profile in straight uniform flow (equation (12)) is not defined at the bed level, a lower integration bound just above the bed has been chosen in equation (20) at z_0. When taking z_0 at $k_s/30 \approx d/30$, the denominator in equation (20) varies from about 145 for $z_0/h = 0.003$ to 215 for $z_0/h = 0.0003$.

[82] This validated model for the curvature-induced increase in production rate $\mathcal{P}$ allows the following:

[83] 1. Gaining insight in the processes underlying the curvature-induced increase in $\mathcal{P}$, which according to equations (19), (20), and (21) is determined by the parameter $C_f^{-1/2}(v_{n,surface}/U)$ that accounts for the dimensionless Chézy coefficient C_f and for the strength of the secondary flow parameterized by $v_{n,surface}/U$. Further development of the model for the curvature-induced production rate of turbulence requires the description of $v_{n,surface}/U$ as a function of depth-averaged flow parameters. For weakly curved flows a linear model for secondary flow (see discussion in section 4.1) gives the following description: $v_{n,surface}/U = (h/R).\text{function}(C_f)$. For moderately to strongly curved flow, however, the use of a nonlinear model is required, such as the one proposed by *Blanckaert and de Vriend* [2003]

$$\frac{v_{n,surface}}{U}\left(C_f, \frac{h}{R}, \beta\right) \xrightarrow{\text{Eq.(4)}} \frac{v_{n,surface}}{U}\left(C_f, \frac{h}{R}, \alpha_s\right) \quad (22)$$

In cases where the parameter α_s (equation (3)) cannot be computed from experimental data, it can be estimated from the velocity redistribution model of *Johannesson and Parker* [1989b]. The elaboration of a 1-D model for the

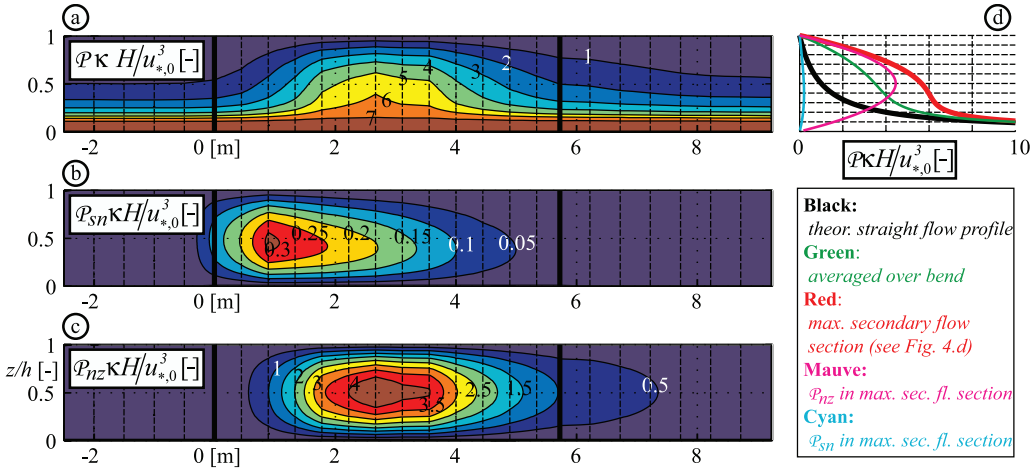

Figure 16. Normalized turbulence production rate in the F16_90_00 experiment according to equation (19). (a) $\mathcal{P}\ \kappa H/u_{*,0}^3$ along the centerline (experimental data in Figure 11b), (b) $\mathcal{P}_{sn}\kappa H/u_{*,0}^3$ along the centerline (experimental data in Figure 14c), (c), $\mathcal{P}_{nz}\kappa H/u_{*,0}^3$ along the centerline (experimental data in Figure 14d). Figures 16a–16c are distorted by a factor 10. (d) Vertical profiles of the normalized turbulence production rate according to the indicated legend.

parameter α_s and subsequently for the parameter $v_{n,surface}/U$ will be reported elsewhere. This model will allow quantifying the influence of the parameters C_f, h/R and α_s.

[84] 2. Further analyzing the relation between curvature-induced energy losses, velocity redistribution, secondary flow, turbulence production rate, and *tke* in the reported experiments. On the basis of equations (19) and (20), the bend-averaged increase in turbulence production rate has been estimated along the centerline as $\langle\mathcal{P}_{\text{bend}}\rangle/\langle\mathcal{P}_{\text{straight}}\rangle \approx$ 1.4, 1.3 and 1.5 in the F11_90_00, F16_90_00 and F21_90_00 experiments, respectively. These values are considerably lower than the experimental estimations of these ratios according to Table 4, which can entirely be attributed to the reduced accuracy in near-bed turbulence measurements that leads to an underestimation of the measured $\mathcal{P}_{\text{straight}}$. Since the secondary flow is maximum on the centerline, the bend averaged value of $\mathcal{P}_{\text{bend}}/\mathcal{P}_{\text{straight}}$ is expected to be lower than the average value along the centerline.

[85] The observations and modeling suggest that the increased energy losses in our experiments can be attributed to two curvature-induced mechanism of comparable importance: the increased boundary shear stress due to the secondary flow and the deformed velocity profiles on the one hand and the increased production rate of turbulence on the other.

[86] 3. Modeling the curvature-induced increase in energy losses in 1-D or 2-D depth-averaged models. When accounting for the turbulence induced increase in energy losses by means of the correction factor

$$\psi_{\text{turbulence}} = \frac{E_{s,\text{bend}}}{E_{s,\text{straight}}} = \frac{\langle\mathcal{P}_{\text{bend}}\rangle}{\langle\mathcal{P}_{\text{straight}}\rangle} \tag{23}$$

computed according to equations (19) and (20), the total curvature-induced energy losses can be modeled as (equations (9), (10), (11))

$$E_s = \psi_{\text{secondary flow}}\psi_{\alpha_s}\psi_{\text{turbulence}}\frac{C_f U^2}{gR_h} \tag{24}$$

The correction factor ψ_{α_s} is computed by depth-averaged 2-D models or modeled according to equation (11) in 1-D models.

[87] 4. Modeling the curvature-induced increase in *tke* in 1-D or 2-D depth-averaged models based on the simplified transport equation for *tke* (equation 8)

$$U\frac{\partial\langle k_{\text{straight}} + \Delta k_{\text{bend}}\rangle}{\partial s} = \langle\mathcal{P}_{\text{straight}} + \Delta\mathcal{P}_{\text{bend}}\rangle - \langle\varepsilon_{\text{straight}} + \Delta\varepsilon_{\text{bend}}\rangle$$
$$\Rightarrow U\frac{\partial\langle\Delta k_{\text{bend}}\rangle}{\partial s} = \langle\Delta\mathcal{P}_{\text{bend}}\rangle - \langle\Delta\varepsilon_{\text{bend}}\rangle \tag{25}$$

Δk_{bend}, $\Delta\mathcal{P}_{\text{bend}}$, and $\Delta\varepsilon_{\text{bend}}$ represent curvature-induced increase in *tke*, turbulence production and turbulence dissipation, respectively. $\langle\Delta\mathcal{P}_{\text{bend}}\rangle$ is modeled by means of equations (19) and (20), whereas $\langle\Delta\varepsilon_{\text{bend}}\rangle$ is modeled in a first-order approximation as follows:

$$\left.\begin{array}{l}\langle\Delta\mathcal{P}_{\text{bend}}\rangle - \langle\Delta\varepsilon_{\text{bend}}\rangle = 0 \text{ in straight reaches}\\ \langle\langle\Delta\varepsilon_{\text{bend}}\rangle\rangle = \langle\langle\Delta\mathcal{P}_{\text{bend}}\rangle\rangle \text{averaged in curved reaches}\\ \langle\Delta\varepsilon_{\text{bend}}\rangle = \text{cte in curved reaches, but } \langle\Delta\varepsilon_{\text{bend}}\rangle \le \langle\Delta\mathcal{P}_{\text{bend}}\rangle\\ \qquad\qquad\qquad\qquad\qquad\qquad\qquad\qquad\text{in first part of bend}\end{array}\right\} \tag{26}$$

The modeled streamwise distributions of $\langle\mathcal{P}_{\text{bend}}\rangle$ and $\langle\varepsilon_{\text{bend}}\rangle$ on the centerline in the F11_90_00, F16_90_00 and F21_90_00 experiments are shown in Figure 17a, whereas Figure 17b compares the streamwise distribution of normalized depth-averaged *tke* $\langle k\rangle/u_{*,0}^2$ from measurements and computed according to model equations (25) and (26).

[88] Comparison of Figures 11d and 12d to Figure 17a shows that the modeled $\langle\mathcal{P}_{\text{bend}}\rangle$ and $\langle\varepsilon_{\text{bend}}\rangle$ are considerably higher than the measured ones. Comparison of Figures 11b and 16a, however, indicates that these differences can be attributed to the important near-bed contribution to $\langle\mathcal{P}_{\text{bend}}\rangle$

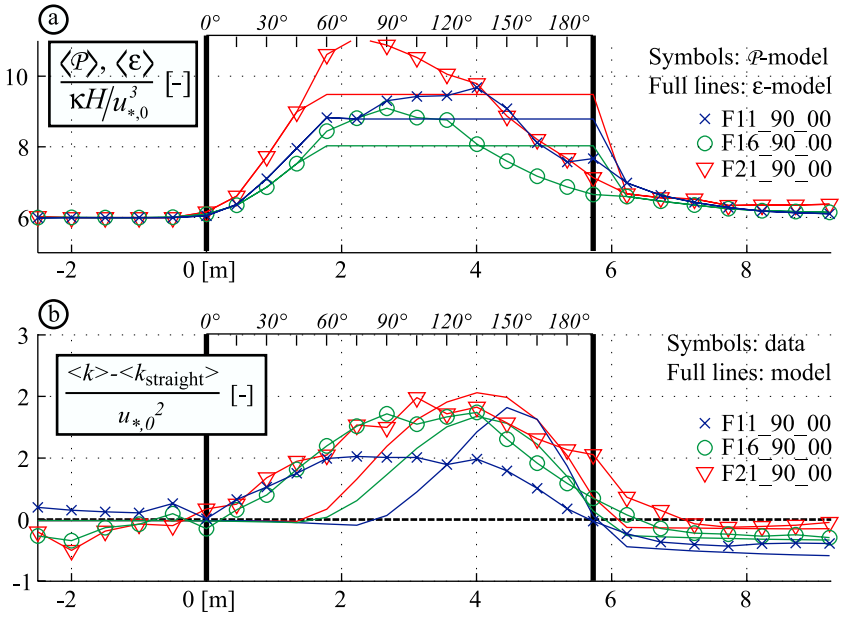

Figure 17. (a) Streamwise distribution along the centerline of the depth-averaged normalized turbulent production rate, $\langle \mathcal{P} \rangle \ \kappa H/u_{*,0}^3$, and turbulent dissipation rate, $\langle \varepsilon \rangle \kappa H/u_{*,0}^3$, according to the model (equations (20) and (26)) in the F11_90_00, F16_9 0_00, and 21_90_00 experiments. (b) Streamwise distribution of normalized depth-averaged turbulent kinetic energy, $\langle k \rangle / u_{*,0}^2$, from measurements (Figure 5) and computed according to equation (25) for the F11_90_00, F16_90_00, and 21_90_00 experiments.

and $\langle \varepsilon_{\text{bend}} \rangle$ which are not resolved by the measurements. The relevance of the proposed model is further confirmed by the satisfactorily reproduction of $\langle \mathcal{P}_{\text{bend}} \rangle$_$\langle \varepsilon_{\text{bend}} \rangle$ (Figure 13a versus Figure 17a). The dissipation $\langle \varepsilon_{\text{bend}} \rangle$ lags behind the production $\langle \mathcal{P}_{\text{bend}} \rangle$ and is attenuated. Figure 17b shows that the modeled curvature-increased *tke* agrees fairly well with the measured one, although model predictions lag somewhat behind measurements. In such a complex 3-D flow, this very simple 1-D model can obviously not be expected to give more than "first-order" estimates of the curvature-induced increase in *tke*.

[89] 5. Since secondary flow drives the model for curvature-induced increase in *tke*, this implies that it enhances mixing and spreading of transported quantities (suspended sediment, heat, oxygen, nutrients, biological species) in two ways: directly by what is commonly called advective mixing [*Fischer*, 1969; *Krishnappan and Lau*, 1977] but also indirectly by increasing the turbulence level, which seems to be a mechanism of dominant order of magnitude in sharp bends. The model for curvature-induced *tke* increase can be extended in a straightforward proportional increase in mixing coefficients.

[90] The further elaboration of the models for the curvature-induced turbulence production rate, energy losses and turbulent kinetic energy, and especially the implementation of *Blanckaert and de Vriend*'s [2003] model for the description of $v_{n,surface}/U$ as a function of depth-averaged flow parameters will be reported elsewhere.

6. Conclusions

[91] This paper reported results from laboratory experiments on sharply curved open-channel flow, carried out in the framework of a broader research program that combines laboratory experiments, field experiments and numerical simulations. Although the laboratory experiments were carried out in a single bend configuration with horizontal bed that is not representative for natural rivers, they yielded some generally valid results.

[92] The paper investigated the adaptation of mean flow and turbulence characteristics to changes in curvature in three experiments with different curvature ratio, H/R. Velocity measurements were made with high spatial and temporal resolution in the vertical plane through the centerline of the flume, allowing to calculate the three time-averaged velocity components, the six Reynolds stresses and the production and dissipation rate of turbulence. These data allowed identifying and visualizing some interesting phenomena, analyzing the underlying hydrodynamic mechanisms and developing models.

6.1. Observed Phenomena

[93] 1. Energy losses increase considerably owing to curvature and are about 40% higher in the investigated sharp bends than in straight flow.

[94] 2. A pronounced secondary flow ($v_n - U_n$) develops in the bend, with maximum transverse velocities that are about 40% of the streamwise velocity.

[95] 3. The vertical profiles of the streamwise velocity (v_s) deform with an increase of velocities in the lower part of the water column.

[96] 4. The *tke* increases strongly in the bend. Its maximum/average values in the reported experiments are about $2.9 \pm 0.5/2.2 \pm 0.2$ times higher than in straight flow. The increase is most pronounced for the transverse fluctuations: the maximum/averaged transverse turbulent normal stresses in the bend are about $4.7 \pm 0.7/3.3 \pm 0.4$ times higher than in straight flow. All turbulent shear stresses are of dominant

order of magnitude in the bend. This curvature-induced increase in turbulence is relevant with respect to spreading and mixing of suspended matter, oxygen or nutrients, temperature, to sediment transport and scour.

[97] 5. The secondary flow, energy losses, and turbulence do not increase proportionally to the curvature ratio H/R, as could be expected on the basis of a linear perturbation approach. The secondary flow and the energy losses are about identical in the three experiments, and the turbulence characteristics only seem to increase weakly. These observations indicate a saturation of curvature effects in very sharply curved open-channel flow.

[98] 6. The recovery length toward straight flow hydrodynamic characteristics seems to increase with the flow depth H.

6.2. Underlying Flow Mechanisms

[99] 1. *Blanckaert and Graf* [2004] and *Blanckaert and de Vriend* [2003] have analyzed and explained the interaction and feedback between streamwise and cross-stream velocities. Advective momentum transport by the secondary flow deforms the v_s profiles, which reduces the driving mechanism of the secondary flow. This nonlinear feedback between v_s and $(v_n - U_n)$ ultimately leads to the observed saturation of the secondary flow for very sharp curvatures.

[100] 2. The analysis of spectral dynamics and of streamwise patterns of turbulence production and dissipation rates suggests the following mechanism underlying curvature-induced increased turbulence. Production and dissipation rates are considerably increased by curvature effects. They are about in equilibrium averaged over the bend, but have different spatial distributions. Production is considerably larger/smaller than dissipation in the first/second half of the bend, leading to an increase/decrease of turbulent kinetic energy. This lagging of the dissipation rate behind the production rate is in line with the energy cascade concept of turbulence. The production rate of turbulence is dominated by the contribution due to the cross-sectional turbulence shear stress $\overline{v_n' v_z'}$ which is closely related to the secondary flow.

[101] 3. The increased energy losses in the bend can be attributed to four mechanisms: (1) the additional transverse component of the boundary shear stress induced by the secondary flow, (2) the increased near-bed gradient of the velocity vector due to the deformed v_s profiles (Figure 3), (3) the increased production rate of turbulence, (4) the nonuniform distribution of the depth-averaged velocity. In the reported experiments, mechanisms 1 and 2 on the one hand and 3 on the other hand were found to be dominant and of comparable magnitude, whereas mechanism 4 was found to be negligible.

[102] It can be concluded that the curvature-induced secondary flow is the dominant mechanism in the reported experiments: it is directly or indirectly responsible for the deformation of the v_s profiles, the curvature-induced increased turbulence production rate, turbulent stresses, *tke* and energy losses. The role of curvature-induced secondary flow is accentuated in the investigated laboratory configurations with rectangular cross section. In sharply curved real rivers, the mobile bed bathymetry is expected to have also an influence of dominant order of magnitude on the characteristics of the turbulence production rate, turbulent stresses, *tke* and energy losses.

6.3. Modeling Implications

[103] 1. *Blanckaert and de Vriend* [2003] have reported a model for the v_s and $(v_n - U_n)$ profiles that accounts for their nonlinear interaction and includes the saturation of the secondary flow in very sharply curved open-channel flow. This model can parameterize curvature effects in 1-D or depth-averaged 2-D hydrodynamic models.

[104] 2. The eddy viscosity concept is shown to represent satisfactorily the turbulent shear stresses, and especially the dominant cross-stream turbulent shear stress $\overline{v_n' v_z'}$ which is closely related to the secondary flow.

[105] 3. On the basis of the eddy viscosity concept and a parameterization of the profiles of streamwise velocity and secondary flow, a model for the curvature-induced increase in turbulence production rate has been developed and validated by means of the reported experimental data. This model quantifies the influence of different geometric and hydraulic parameters and identifies $(C_f^{-1/2} v_{n,surf}/U)$ as the dominant scaling parameter.

[106] 4. Correction factors to the friction factor that parameterize curvature-induced increase in energy losses have been derived. They account for curvature-induced turbulence production rate, secondary flow and the nonuniformity of the velocity distribution.

[107] 5. On the basis of the model for curvature-induced increase in turbulence production rate, a 1-D model is developed for the curvature-induced increase in *tke* and mixing.

[108] Owing to limitations in computational capacity, long-term (scale of a flood event to geological scales) or large-scale (scale of a river basin) investigations make use of 1-D or 2-D depth-averaged morphodynamic models. As aforementioned, such models are currently unable to describe curvature-induced turbulence and energy losses, and they are limited to a simplified parameterization of the time-averaged flow based on a model for secondary flow which validity is limited to low and moderate curvatures. The here reported results allow enhancing existing 1-D or 2-D depth-averaged morphodynamic models by extending the validity range to sharp curvatures and by including a parameterization for curvature-induced increase in energy losses, *tke* and mixing. These extensions may improve the models' predictive capacity and reliability in multiple applications. A better understanding and modeling of the investigated processes may lead to more accurate estimations of the boundary shear stress, the sediment transport, the conveyance capacity and the water quality, a better assessment of natural hazards and the development of less expensive and more environmentally friendly bank protection measures as well as river restoration schemes that can guarantee the conservation of biodiversity. The extension of the validity range to sharp curvatures is important with respect to meander dynamics, and especially with respect to the modeling of cutoff events and the accompanying local restraightening. The frequency of occurrence of these events determines the rate of floodplain rejuvenation as well as the sedimentologic structure of the meander belt. The former is an important ecological parameter, whereas knowledge of the latter is required for the sustainable exploitation of drinking water of hydrocarburates.

[109] Beside enhancing insight in the hydrodynamics of sharply curved open-channel flow and improving modeling

tools, the reported data are useful for the validation of numerical codes. More data from the reported experiments and from other experiments (Blanckaert, submitted manuscript, 2009) can be obtained from the author.

[110] **Acknowledgments.** This research was supported by the Swiss National Science Foundation under grants 2100-052257.97 and 2000-059392.99 and by the Netherlands Organization for Scientific Research (NWO) under grant DN66-149. The author wishes to acknowledge W. H. Graf, H. J. de Vriend, and W. S. J. Uijttewaal as well as R. Ferguson, A. Sukhodolov, M. Garcia, and an anonymous reviewer for constructive comments that improved the manuscript.

References

Andrle, R. (1994), Flow structure and development of circular meander pools, *Geomorphology*, *9*, 261–270, doi:10.1016/0169-555X(94)90049-3.

Argawal, V. C., R. J. Garde, and K. G. Ranga Raju (1984), Resistance to flow and sediment transport in curved alluvial channels, paper presented at 4th Congress, IAHR- APD, Chiang Mai, Thailand.

Bagnold, R. A. (1960), Some aspects of the shape of river meanders, *U.S. Geol. Surv. Prof. Pap., 282E*135–144.

Batchelor, G. K. (1967), *An Introduction to Fluid Dynamics*, Cambridge Univ. Press, Cambridge, U. K.

Bathurst, J. C., C. R. Thorne, and R. D. Hey (1979), Secondary flow and shear stress at river bends, *J. Hydraul. Div. Am. Soc. Civ. Eng.*, *105*(10), 1277–1295.

Biedenharn, D. S., P. G. Combs, G. J. Hill, C. F. J. Pinkard, and C. B. Pinkston (1989), Relation between channel migration and radius of curvature on the Red river, in *Sediment Transport Modeling: Proceedings of the International Symposium*, edited by S. Y. Sam Wang, pp. 536–541, Am. Soc. of Civ. Eng., New York.

Blanckaert, K., and H. J. de Vriend (2003), Nonlinear modeling of mean flow redistribution in curved open channels, *Water Resour. Res.*, *39*(12), 1375, doi:10.1029/2003WR002068.

Blanckaert, K., and H. J. de Vriend (2004), Secondary flow in sharp open-channel bends, *J. Fluid Mech.*, *498*, 353–380, doi:10.1017/S0022112003006979.

Blanckaert, K., and W. H. Graf (2001), Experiments on flow in an open-channel bend: Mean flow and turbulence, *J. Hydraul. Eng.*, *127*(10), 835–847, doi:10.1061/(ASCE)0733-9429(2001)127:10(835).

Blanckaert, K., and W. H. Graf (2004), Momentum transport in sharp open-channel bends, *J. Hydraul. Eng.*, *130*(3), 186–198, doi:10.1061/(ASCE)0733-9429(2004)130:3(186).

Blanckaert, K., and U. Lemmin (2006), Means of noise reduction in acoustic turbulence measurements, *J. Hydraul. Res.*, *44*(1), 3–17.

Crosato, A. (2008), Analysis and modelling of river meandering, Ph.D. thesis, Delft Univ. of Technol., Delft, Netherlands.

de Vriend, H. J. (1977), A mathematical model of steady flow in curved shallow channels, *J. Hydraul. Res.*, *15*(1), 37–54.

de Vriend, H. J. (1981), Steady flow in shallow channel bends, *Rep. 81–3*, Fluid Mech. Lab., Dept. of Civ. Eng., Delft Univ. of Technol, Delft, Netherlands.

Edwards, B. F., and D. H. Smith (2002), River meandering dynamics, *Phys. Rev. E*, *65*, 1–12.

Engelund, F. (1974), Flow and bed topography in channel bends, *J. Hydraul. Div. Am. Soc. Civ. Eng.*, *100*(HY11), 1631–1648.

Ferguson, R. I., D. R. Parsons, S. N. Lane, and R. J. Hardy (2003), Flow in meander bends with recirculation at the inner bank, *Water Resour. Res.*, *39*(11), 1322, doi:10.1029/2003WR001965.

Fischer, H. B. (1969), Effects of bends on dispersion in streams, *Water Resour. Res.*, *5*, 496–506, doi:10.1029/WR005i002p00496.

Furbish, D. J. (1988), River-bend curvature and migration: How are they related?, *Geology*, *16*(8), 752–755, doi:10.1130/0091-7613(1988)016<0752:RBCAMH>2.3.CO;2.

Graf, W. H., and M. Altinakar (1998), *Fluvial Hydraulics: Flow and Transport Processes in Channels of Simple Geometry*, John Wiley, Chichester, U. K.

Hickin, E. J. (1974), The development of meanders in natural river-channels, *Am. J. Sci.*, *274*, 414–442.

Hickin, E. J., and G. C. Nanson (1975), The character of channel migration on the Beatton river, northeast British Columbia, Canada, *Geol. Soc. Am. Bull.*, *86*, 487–494, doi:10.1130/0016-7606(1975)86<487:TCOCMO>2.0.CO;2.

Hinze, J. O. (1975), *Turbulence*, McGraw-Hill, New York.

Hooke, J. M. (1987), Changes in meander morphology, in *International Geomorphology 1986 Part I*, edited by V. Gardiner, pp. 591–609, John Wiley, Chichester, U. K.

Hurther, D., and U. Lemmin (1998), A constant beamwidth transducer for three-dimensional Doppler profile measurements in open channel flow, *Meas. Sci. Technol.*, *9*(10), 1706–1714, doi:10.1088/0957-0233/9/10/010.

Hurther, D., and U. Lemmin (2001), A correction method for turbulence measurements with a 3-D acoustic Doppler velocity profiler, *J. Atmos. Oceanic Technol.*, *18*, 446–458, doi:10.1175/1520-0426(2001)018<0446:ACMFTM>2.0.CO;2.

Ikeda, S., G. Parker, and K. Sawai (1981), Bend theory of river meanders. Part 1. Linear development, *J. Fluid Mech.*, *112*, 363–377, doi:10.1017/S0022112081000451.

Johannesson, H., and G. Parker (1989a), Secondary flow in a mildly sinuous channel, *J. Hydraul. Eng.*, *115*(3), 289–308.

Johannesson, H., and G. Parker (1989b), Velocity redistribution in meandering rivers, *J. Hydraul. Eng.*, *115*(8), 1019–1039.

Kikkawa, H., S. Ikeda, and A. Kitagawa (1976), Flow and bed topography in curved open channels, *J. Hydraul. Div. Am. Soc. Civ. Eng.*, *102*(HY9), 1327–1342.

Krishnappan, B. G., and Y. L. Lau (1977), Transverse mixing in meandering channels with varying bottom topography, *J. Hydraul. Res.*, *15*(4), 351–371.

Lancaster, S. T., and R. L. Bras (2002), A simple model of river meandering and its comparison to natural channels, *Hydrol. Processes*, *16*, 1–26, doi:10.1002/hyp.273.

Leeder, M. R., and P. H. Bridges (1975), Flow separation in meander bends, *Nature*, *253*(5490), 338–339, doi:10.1038/253338a0.

Lemmin, U., and T. Rolland (1997), Acoustic velocity profiler for laboratory and field studies, *J. Hydraul. Eng.*, *123*(12), 1089–1098.

Leopold, L. B., R. A. Bagnold, M. G. Wolman, and L. M. Brush (1960), Flow resistance in sinuous and irregular channels, *U.S. Geol. Surv. Prof. Pap., 282D*, 111–134.

Liverpool, T. B., and S. F. Edwards (1995), Dynamics of a meandering river, *Phys. Rev. Lett.*, *75*(16), 3016–3019.

Markham, A. J., and C. R. Thorne (1992), Geomorphology of gravel-bed river bends, in *Dynamics of Gravel-Bed Rivers*, edited by P. Billi et al., pp. 433–456, John Wiley, New York.

Mockmore, C. A. (1943), Flow around bends in stable channels (including discussions), *Trans. Am. Soc. Civ. Eng.*, *109*, 593–628.

Nanson, G. C., and E. J. Hickin (1986), A statistical analysis of bank erosion and channel migration in western Canada, *Geol. Soc. Am. Bull.*, *97*, 497–504, doi:10.1130/0016-7606(1986)97<497:ASAOBE>2.0.CO;2.

Nezu, I., and H. Nakagawa (1993), *Turbulence In Open-Channel Flows*, Balkema, Rotterdam, Netherlands.

Odgaard, A. J. (1981), Transverse bed slope in alluvial channel bends, *J. Hydraul. Div. Am. Soc. Civ. Eng.*, *107*(HY12), 1677–1694.

Odgaard, A. J. (1982), Bed characteristics in alluvial channel bends, *J. Hydraul. Div. Am. Soc. Civ. Eng.*, *108*(HY11), 1268–1281.

Odgaard, A. J. (1984), Flow and bed topography in alluvial channel bends, *J. Hydraul. Eng.*, *110*(4), 521–536, doi:10.1061/(ASCE)0733-9429(1984)110:4(521).

Odgaard, A. J. (1986), Meander flow model. I: Development, *J. Hydraul. Eng.*, *112*(12), 1117–1136, doi:10.1061/(ASCE)0733-9429(1986)112:12(1117).

Onishi, Y., S. C. Jain, and J. F. Kennedy (1972), Effects of meandering on sediment discharges and friction factors of alluvial streams, *Rep. 141*, Iowa Inst. of Hydraul. Res., pp. 1–150.

Parker, G., and E. D. Andrews (1986), On the time development of meander bends, *J. Fluid Mech.*, *162*, 139–156, doi:10.1017/S0022112086001970.

Parker, G., K. Sawai, and S. Ikeda (1982), Bend theory of river meanders. Part 2. Nonlinear deformation of finite-amplitude bends, *J. Fluid Mech.*, *115*, 303–314, doi:10.1017/S0022112082000767.

Parker, G., P. Diplas, and J. Akiyama (1983), Meander bends of high amplitude, *J. Hydraul. Eng.*, *109*(10), 1323–1337, doi:10.1061/(ASCE)0733-9429(1983)109:10(1323).

Rozovskii, I. L. (1957), *Flow of Water in Bends of Open Channels*, Acad. of Sci. of the Ukrainian SSR, Kiev. (Isr. Program for Sci. Transl., Jerusalem, 1961.)

Seminara, G. (2006), Meanders, *J. Fluid Mech.*, *554*, 271–297, doi:10.1017/S0022112006008925.

Seminara, G., and M. Tubino (1992), Weakly nonlinear theory of regular meanders, *J. Fluid Mech.*, *244*, 257–288, doi:10.1017/S0022112092003069.

Shiono, K., Y. Muto, D. W. Knight, and A. F. L. Hyde (1999), Energy losses due to secondary flow and turbulence in meandering channels with overbank flows, *J. Hydraul. Res.*, *37*(5), 641–664.

Stølum, H.-H. (1996), River meandering as a self-organization process, *Science*, *271*, 1710–1713, doi:10.1126/science.271.5256.1710.

Stølum, H.-H. (1998), Planform geometry and dynamics of meandering rivers, *Geol. Soc. Am. Bull.*, *110*(11), 1485–1498, doi:10.1130/0016-7606(1998)110<1485:PGADOM>2.3.CO;2.

Struiksma, N., K. W. Olesen, C. Flokstra, and H. J. de Vriend (1985), Bed deformation in curved alluvial channels, *J. Hydraul. Res.*, *23*(1), 57–79.

Sun, T., P. Meakin, T. Jøssang, and K. Schwarz (1996), A simulation model for meandering rivers, *Water Resour. Res.*, *32*, 2937–2954, doi:10.1029/96WR00998.

van Bendegom, L. (1947), Eenige beschouwingen over riviermorphologie en rivierverbetering (in Dutch), *De Ingenieur*, *59*(4), 1–11.

van Rijn, L. C. (1984), Sediment transport. Part III: Bed forms and alluvial roughness, *J. Hydraul. Eng.*, *110*(12), 1733–1754.

Zeng, J., G. Constantinescu, K. Blanckaert, and L. Weber (2008), Flow and bathymetry in sharp open-channel bends: Experiments and predictions, *Water Resour. Res.*, *44*, W09401, doi:10.1029/2007WR006303.

K. Blanckaert, ENAC, Ecole Polytechnique Fédérale, CH-1015 Lausanne, Switzerland. (koen.blanckaert@epfl.ch)